Chemical Engineering Journal 498 (2024) 155370

Contents lists available at ScienceDirect

Chemical Engineering Journal

journal homepage: www.elsevier.com/locate/cej

Synergistic Triple-Action morphological composite Anode: Integrating lattice Softening, Interfacial electric Fields, and dual confinement for superior Potassium-Ion battery performance

Jia-Sheng Lin [a], Yi-Yen Hsieh [a], Kai-Yuan Hsiao [b], Yi-Chun Yang [a], Che-Hung Wang [c], Ming-Yen Lu [b], Wen-Wei Wu [c], Hsing-Yu Tuan [a,*]

[a] Department of Chemical Engineering, National Tsing Hua University, Hsinchu 30013, Taiwan
[b] Department of Materials Science and Engineering, National Tsing Hua University, Hsinchu 30013, Taiwan
[c] Department of Materials Science and Engineering, National Chiao Tung University, Hsinchu 30010, Taiwan

ARTICLE INFO

Keywords:
Potassium ion battery
Dual confinement
Synergistic effect
Bond softening effect
P-n junction

ABSTRACT

Synergistic effects could significantly improve slow redox kinetics and structural pulverization of electrodes in potassium ion batteries (PIBs); however, the performance of single synergistic designs is limited. Multi-synergistic composite, shaped by a blend of factors, substantially boosts performance, yielding outcomes that surpass single synergistic coupling design. Herein, we develop a Bi_2Se_3/Sb_2Se_3@NC@G electrode that integrates three key features for enhanced potassium-ion storage: p-n junctions enhance electron transfer through internal electric fields, dual confinement prevents K_2Se dissolution into the electrolyte, and lattice softening in the Bi-Sb alloy relieves stress during potassium ion insertion/extraction. These multi-synergistic effects enable the heterostructure to exhibit superior electrochemical performance in potassium-ion batteries. The Bi_2Se_3/Sb_2Se_3@NC@G electrode demonstrates notable capacity of 640 mA h g^{-1} at current density of 50 mA g^{-1}, achieving 95.5 % of its theoretical capacity, maintain stable capacity of 310 mA h g^{-1} after 5000 cycles at current density of 0.5 A/g with 0.002 % per cycle degradation, and exhibits the fastest rate capability up to 10 A/g (172 mA h g^{-1}). Furthermore, potassium ion hybrid capacitor (PIHC) can achieve a high energy density of 118 Wh kg^{-1} and a power density of 5200 W kg^{-1}, and full cell shows an attractive energy density of 97 Wh kg^{-1} and a stable performance after 250 cycling number under 1 A g^{-1}. This study proposes an effective strategy that employs multiple synergistic coupling designs to maximize potassium-ion storage capacity, achieving a breakthrough in extending battery lifecycle.

1. Introduction

Developing advanced energy storage technologies beyond lithium-ion batteries (LIBs) is increasingly urgent for sustainable, low-cost, large-scale solutions [1–3]. Potassium-ion batteries (PIBs) have emerged as a promising alternative, offering close oxidation–reduction potentials to LIBs (K: −3.04 V, Li: −2.93 V), which suggests a high energy density potential[4,5]. However, PIBs confront considerable challenges, primarily slow redox kinetics and structural pulverization due to the large radius of K^+, thus leading to rapid capacity decay and inadequate cycling stability [2,6–8]. To overcome these obstacles, recent progress focus on improving electrode materials and electrolyte compositions. Enhanced electrode designs aim to accommodate K^+ better, reducing volumetric expansion and structural degradation during charge cycles. Simultaneously, electrolyte modifications seek to increase ionic conductivity and stabilize electrode interfaces, crucial for extending battery life and enhancing performance. These advancements are critical for realizing the full potential of PIBs in practical energy storage applications.

The anode materials utilized in PIBs can be classified into three distinct types: intercalation-type, alloying-type, and conversion-type, each characterized by unique electrochemical properties and challenges [9–14]. Intercalation-type materials, despite extensive investigation, often exhibit limited active sites and insufficient capacity, consequently constraining the battery's overall energy density [15]. On the other hand, alloying-type and conversion-type anodes, which

* Corresponding author.
E-mail address: hytuan@che.nthu.edu.tw (H.-Y. Tuan).

https://doi.org/10.1016/j.cej.2024.155370
Received 31 May 2024; Received in revised form 25 July 2024; Accepted 29 August 2024
Available online 3 September 2024

facilitate multi-electron transfer reactions, have garnered significant attention due to their potential in enhancing mass energy density. These materials primarily include transition metal oxides (TMOs), sulfides (TMSs), and selenides (TMSes). The mass energy density of electrode materials can be calculated using the extended Nernst equation [16,17]:

$$E_D = \frac{\Delta_r G^{\theta}}{\sum M_i} = -\frac{nFE}{\sum M_i}$$

Here, n represents the number of charges transferred per mole of reaction, F is the Faraday constant, E represents the thermodynamic equilibrium voltage or electromotive force (emf), and ΣM_i is the sum of the mole weights or mole volumes of the reactants. Notably, the Gibbs formation energy, which significantly impacts reactivity and energy density, can be derived from first-principles calculations, emphasizing the reaction's dependence on electron transfer mechanisms. Alloying and conversion-type anodes face critical challenges during operation. Significant volume expansions during the charge and discharge cycles often lead to material aggregation and pulverization, thereby impeding electrical contact and slowing reaction kinetics. Furthermore, these materials are prone to the formation of solid electrolyte interface (SEI) layers, which are initially unstable and can dissolve, thus diminishing the Coulombic efficiency—a paramount factor for practical applications. Addressing these issues, various strategies like synergistic effects, morphology control, and conductive substrates have been employed to enhance structural stability and electrochemical performance [18–21]. For example, morphological modifications have proven effective in facilitating potassium ion diffusion and improving electron transfer, both of which are essential for high-performance PIBs. Techniques such as Cu doping in SnSe have been shown to alter local charge distributions and improve interlayer binding energy, significantly enhancing the electrochemical stability of the materials [22]. Additionally, the construction of ZnTe/$CoTe_2$ heterostructures exemplifies how strategic design can lead to superior electrochemical storage capabilities [23]. Despite the advancements in material design and strategic enhancements, the overall capacity of these electrodes remains limited by the inherent specific capacities of the substrates, such as carbon materials, which typically exhibit lower specific capacities (e.g., KC_8 = 279 mA h g^{-1}) [24,25]. Thus, while strategies like the introduction of conductive substrates increase cycling stability, they simultaneously decrease the electrode's total capacity. Moreover, although the lattice softening effect in Bi-Sb nanograins forms stable intermediate phases that exhibit lower expansion rates, these advancements do not fully resolve the issues related to cyclic stability [26].

The multi-synergistic composite, influenced by a combination of factors, significantly enhances performance, achieving results greater than the sum of its parts [27,28]. Extensive potential applications are evident across diverse sectors such as automotive manufacturing, medical devices, and infrastructure and construction. These composites demonstrate nonlinear cumulative impacts, where interactions between two active ingredients produce superior outcomes, either through similar or sequential activities. In the context of PIBs, the application of multi-synergistic composites involves integrating various strategies into material design, thereby elevating electrochemical performance. Multi-element compounds are attractive because of their diverse compositions, adaptable crystal structures, and distinctive morphologies, which bestow excellent physical, chemical, optical, and electronic properties [29,30]. The synergistic interaction of these multicomponent properties makes them highly promising for applications in electrochemical energy storage. In recent years, encapsulating carbon materials has been a widely employed approach to achieve synergistic effects across various battery systems and material designs. This method can yield diverse outcomes. For instance, Hu et al. designed a ZnTe@C/Ti_3C_2Tx (ZCT) nano-hybrid material [31], demonstrating outstanding long-term cycling performance over 3500 cycles, surpassing a single carbon-coated ZnTe@C counterpart. Carbon coating enhances charge transfer and strengthens electrode structural stability. Dual confinement can combine carbon hosts of different dimensions, achieving remarkable electrical conductivity and significant cycling performance [32,33]. In potassium–selenium batteries, hollow carbon spheres promote electrolyte penetration and provide fast transfer channels, playing a synergistic role.

In this study, a novel composite material composed of Bi_2Se_3/Sb_2Se_3 p-n junction heterostructure material and carbon materials (N-doped carbon and graphene) has been developed, named Bi_2Se_3/Sb_2Se_3@NC@G, aiming to achieve high-performance potassium ion energy storage systems. The synergistic triple-action morphological composite anode is designed based on nanonetwork $BiSbO_4$ selenization and carbonization, featuring a regularly stacked design, with nanosheets of Bi_2Se_3 attached to nanorods of Sb_2Se_3. We introduce the three main concepts of p-n junction, bond softening, and dual confinement into the Sb_2Se_3 system to achieve highly reversible stable cycling (Scheme 1). First, due to the difference in band structure and electron concentration, leading to charge redistribution, an internal electric field is spontaneously generated, accelerating the diffusion capacity of electrons/ions and enhancing charge transfer in electrode materials. The abundant heterojunctions effectively improve the reaction kinetics, benefiting excellent high-rate performance [34]. Second, through the introduction of dual confinement, the synergistic effect between the design of p-n junction heterostructure and dual-layer carbon materials creates effective electron transport channels, and the framework effectively alleviates the large volume expansion of Sb during potassium insertion/extraction processes, preventing K_2Se dissolution into the electrolyte and consequent shuttle effect during long-term cycling [35,36]. Third, the chemical properties of lattice softening in Bi-Sb alloy can mitigate the relevant stresses during potassium ion insertion/extraction processes, thereby suppressing volume expansion and achieving highly reversible stable cycling [26]. By maximizing the multi-synergistic effects, we demonstrate the technical feasibility and engineering approach of electrode design for potassium ion energy storage systems.

2. Experimental Section

2.1. Materials

Bismuth(III) nitrate pentahydrate ($Bi(NO_3)_3{\cdot}5H_2O$, reagent grade, 98%), *hexa*-decyltrimethylammonium bromide (CTAB, for molecular biology, 99%), Selenium (powder, 325 mesh, 99.5%), dopamine hydrochloride ($(HO)_2C_6H_3CH_2NH_2{\cdot}HCl$), 2-Amino-2-(hydroxymethyl)-1,3-propane-diol ($NH_2C(CH_2OH)_3$, ACS reagent grade,≧99.8%), dimethyl ether (DME, anhydrous 99.5%), dimethyl carbonate (DMC, anhydrous 99%), and potassium metal (chunks in mineral oil, 98%) were purchased from Sigma-Aldrich. Antimony (III) oxide (Sb_2O_3, 99%) were purchased from Alfa-Aesar. Potassium bis(fluorosulfonyl)imide (KFSI, 97%) was purchased from Combi-Blocks. Sodium carboxymethyl cellulose (NaCMC, average $M_w \sim 700{,}000$), Super-P and coin-type cell CR2032 were purchased from shining energy. Active carbon (AC) was purchased from Kuraray Chemical. Glass fiber was purchased from Advantec. Copper and aluminum foil were purchased from Chang-Chun group. All chemicals were used directly with no additional purification.

2.2. Material characterization

The morphologies of the obtained samples were investigated using scanning electron microscopy (SEM, Hitachi SU8010) equipped with energy-dispersive X-ray spectroscopy (EDS) detector. Transmission electron microscopy (TEM) (JEOL, JEM-ARM200FTH, serviced provided by NTHU) with an accelerating voltage of 200 kV for investigating structural analysis including morphology, crystal lattice spacing, and selected-area electron diffraction (SAED). The structural evolution and composition were identified using X-ray diffraction (Bruker, D8 ADVANCE) with Cu-Kα radiation (λ = 1.54 Å) and the oxidation states

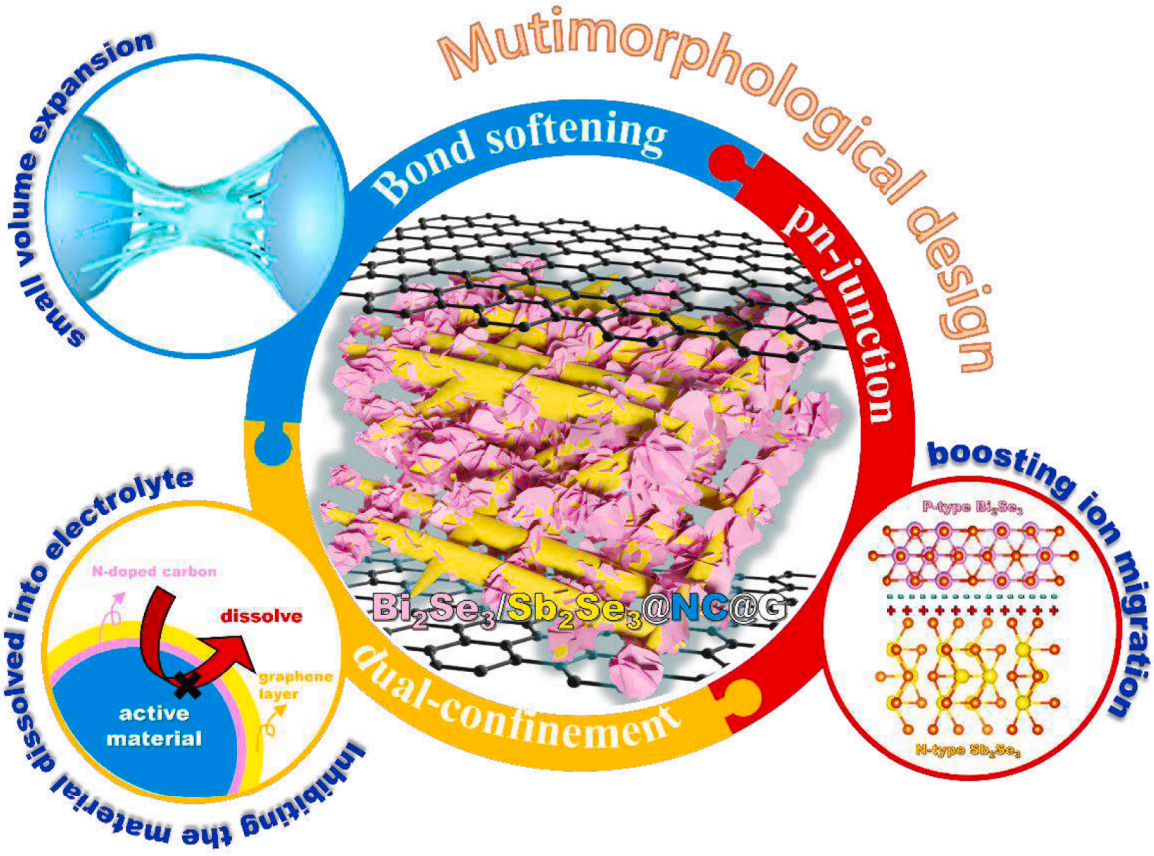

Scheme 1. Schematic illustration of the synergistic triple-action concepts of Bi_2Se_3/Sb_2Se_3@NC@G composites.

of the samples were characterized by high-resolution Xray photoelectron spectrometer (XPS, ULVAC-PH, PHI QuanteraII, NTHU). All the spectra obtained from XPS analysis were first calibrated by referencing the standard binding energy of C 1 s (284.8 eV), followed by the curve fitting using the software of XPSPEAK VER. 4.1. The ultraviolet photoelectron spectroscopy (UPS, ULVAC PHI 5000 Versa Probe, serviced provided by NTU) and UV–vis (Aglient, serviced provided by NTNU) spectra are used for confirming the valence band and energy gap. Thermogravimetric analysis was performed using a thermogravimetric analyzer (TA, Q50) in the atmosphere with a temperature ramp rate of 10 °C min^{-1} and a temperature range of 25–800 °C. Raman spectroscopy was performed using a Micro Raman Identify Dual (MRID). Surface area was detected by Brunauer–Emmett–Teller (BET) method.

2.3. Fabrication of $BiSbO_4$ nanonetworks

The $BiSbO_4$ nanonetworks were prepared by hydrothermal method. The aqueous CTAB solution was prepared by adding 0.075 g of CTAB into a serum bottle with 25 mL of deionized water via constant stirring (500 rpm) for 30 min. Thereafter, 485.1 mg $Bi(NO_3)_3{\cdot}5H_2O$ and 145.8 mg Sb_2O_3 were added into the serum bottle. The mixture was transferred into 50 mL Teflon autoclave at 170 °C for 24h. The obtained solution was collected by centrifugation (5 min per cycle at 8000 rpm) three times using absolute ethanol and deionized water.

2.4. Fabrication of Bi_2Se_3/Sb_2Se_3@NC

50 Mg as-prepared $BiSbO_4$ nanonetworks was dispersed into a tris-buffer solution (10 mmol, 50 mL) by sonication for 2 h, 25 mg dopamine hydrochloride (DA. HCl) was subsequently added into the solution and vigorously stirred for 4 h. The black $BiSbO_4$@PDA precursor powder was collected by rinsing thoroughly with deionized water several times. $BiSbO_4$@PDA (100 mg) and Se powder (600 mg) were put into a quartz boat and annealed under Ar atmosphere at 500°C for 7.5h (3°C min) to obtain Bi_2Se_3/Sb_2Se_3@NC

2.5. Fabrication of Bi_2Se_3/Sb_2Se_3@NC@G

The Bi_2Se_3/Sb_2Se_3@NC@G composites were synthesized via high energy mechanical milling. Bi_2Se_3/Sb_2Se_3@NC and graphene (the mass ratio was 3:1) were placed into a stainless-steel jar with stainless-steel balls and sealed inside an argon-filled glovebox. The mass ratio of ball to powder is about 180:1. Finally, the mixture was ball milled for 24 h. For comparison, the Bi_2Se_3@NC@G and Sb_2Se_3@NC@G were synthesized by a similar method.

2.6. Electrochemical measurement

These electrodes were prepared by mixing the active material (Bi_2Se_3/Sb_2Se_3@NC@G 70%), super-P carbon black (20%), and NaCMC (10%) in DI water to form a uniform slurry. The homogeneous slurry was coated onto the copper foil and dried under vacuum at 80 °C for 1 h in a

furnace to remove the residual solvent. The mass loading of active material in Bi_2Se_3/Sb_2Se_3@NC@G are 0.7∼0.9 mg cm^{-2}. For electrochemical test, the half cells were assembled with the potassium foil as the counter electrode, a solution of 4 M KFSI in DME as electrolyte, and glass fiber filters (Advantec.) as a separator. CR2032 coin cells were assembled in an argon-filled glove box with both the moisture and the oxygen content bellow 1 ppm (M. Braun UNILAB). Galvanostatic charge/discharge tests were evaluated by NEWARE CT-4000 battery measurement system from 0.01 to 3.0 V vs. K^+/K. Galvanostatic intermittent titration technique (GITT) were evaluated by Maccor Series 4000 battery test system. Cyclic voltammetry (CV) and electrochemical impedance spectroscopy (EIS) curves were obtained on Bio-Logic-Science Instruments, VMP3 workstation. EIS was set with a potential window of 0.01–3.00 V and a frequency of 600 kHz to 50 kHz. For Mott–Schottky measurements, the Bi_2Se_3/Sb_2Se_3@NC were employed as working electrodes, while Ag/AgCl and Pt were used as the reference and counter electrode, respectively. The Mott–Schottky plots were carried out in 0.5 M Na_2SO_4 aqueous solution.

2.7. Potassium-ion full cell of Bi_2Se_3/Sb_2Se_3@NC@G//Prussian blue (PB)

The CR2032 potassium-ion coin type full cell was assembled by setting the cathode-to-anode overall surface charge ratio to be 1. Before full cell assembly, PB was prepotassiated for 23 cycles. The working window of PB is set between 2.0 V ∼ 4.0 V and discharge to 2.0 V. Bi_2Se_3/Sb_2Se_3@NC@G was prepotassiated for 23 cycles. The working window of Bi_2Se_3/Sb_2Se_3@NC@G is set between 0.01 V ∼ 3.0 V and discharge to 0.01 V. For full cell assembly, the working window for full cell is set between 1.0 V ∼ 3.8 V and the electrolyte used in the cells was 1M KFSI in DMC.

2.8. Potassium-ion hybrid capacitor (PIHC) of Bi_2Se_3/Sb_2Se_3@NC@G// AC

The PIHC was assembled by using Bi_2Se_3/Sb_2Se_3@NC@G for anode and active carbon for cathode, with an overall mass ratio to be 1. Before the hybrid capacitor assembly, the anode was prepotassiated for 23 cycles and discharge to 0.01 V. The working window for the hybrid capacitor is 0.01 V ∼ 3.8 V.

2.9. DFT calculation

The DFT as implemented in the Vienna Ab initio simulation package (VASP) in all calculations [37]. The exchange–correlation potential is described by using the generalized gradient approximation of Perdew-Burke-Ernzerhof (GGA-PBE) [38]. The projector augmented-wave (PAW) method is employed to treat interactions between ion cores and valence electrons [39]. The plane-wave cutoff energy was fixed to 450 eV. Given structural models were relaxed until the Hellmann–Feynman forces smaller than −0.02 eV $Å^{-1}$ and the change in energy smaller than 10^{-5} eV was attained. Grimme's DFT-D3 methodology was used to describe the dispersion interactions among all the atoms in adsorption models.

2.10. Finite element analysis (FEA) simulation

Finite element simulation using the Structural Mechanics Module of COMSOL Multiphysics software, a simulation is constructed for two different material structures in a microscopic 3D form. Due to the expansion stress brought about by embedded reactions, the implicit computation mode calculates the stress and strain caused by expansion in the rod material. The overall conservation equations comply with Newton's second law. For both structures, the expansion rate due to the reaction is applied to the strain of the rod material in the form of interlayer strain, simulating the expansion of the rod. The outermost boundaries are set as fixed boundaries. For the mass transfer process, a simplified rod array structure at the local region of the interface with the electrolyte was constructed. A free mass transfer simulation model based on Fick's law was developed, which simulates mass transfer using the diffusion equation. The top boundary is set as a relative concentration boundary with a relative concentration of 1, while the other outer boundaries are set as no-diffusion boundaries.

3. Results and discussion

Multi-synergistic composite Bi_2Se_3/Sb_2Se_3@NC@G were synthesized via a four-step reaction: hydrothermal synthesis of a $BiSbO_4$ nanonetwork (Fig. S1), followed by a polydopamine (PDA) coating, and concluding with a thermal selenization treatment and a ball milling method [40–42]. In an alkaline environment, dopamine self-polymerizes in a tris-buffer solution to form a uniform PDA layer on the $BiSbO_4$ nanonetwork, creating $BiSbO_4$@PDA. This template underwent thermal selenization with Se powder in a tube furnace, producing the multi-synergistic composite Bi_2Se_3/Sb_2Se_3@NC. At the end, Bi_2Se_3/Sb_2Se_3@NC was mixed with graphene to form Bi_2Se_3/Sb_2Se_3@NC@G. SEM analysis (Fig. 1b) revealed a composite structure of rod-shaped Sb_2Se_3 and plate-like Bi_2Se_3 with a rough surface from in-situ form n-doped carbon[43]. X-ray diffraction (XRD) analysis confirmed the material's crystalline phases (Fig. 1c), with overlapping peaks for rhombohedral Bi_2Se_3 (R-3m (166), JCPDS No. 00–033-0214) and orthorhombic Sb_2Se_3 (Pnma (62), JCPDS No. 01–075-1462), indicating the coexistence of both phases without impurities. Fig. 1d shows crystal structure of Bi_2Se_3/Sb_2Se_3. TEM observations (Fig. 1e) showed a dendritic structure with rod-shaped Sb_2Se_3 and wrapped plate-like Bi_2Se_3, forming a three-dimensional structure that prevents self-aggregation and buffers volume expansion during potassium ion insertion/extraction. SEM images (Fig. S3) depict Bi_2Se_3 synthesized via hydrothermal synthesis with a dopamine and carbon coating, preserving its layered structure. This is evidenced in Fig. S4, which shows rod-shaped Sb_2Se_3@NC. Fig. S5 illustrates Bi_2Se_3/Sb_2Se_3 @NC@G after ball milling, fully encapsulated by graphene. HRTEM images of Bi_2Se_3/Sb_2Se_3@NC@G (Fig. S6) confirm a double-layer carbon structure, featuring an outer graphene layer from ball milling and an inner layer of amorphous n-doped carbon [44]. To distinguish the morphology of the Bi_2Se_3/Sb_2Se_3@NC, Fig. S7 show the morphology of the Bi_2Se_3/Sb_2Se_3@NC, Sb_2Se_3@NC nanorod and Bi_2Se_3@NC nanosheets. Fig. S7a exhibit the Sb_2Se_3 nanorods are covered with the Bi_2Se_3 nanosheets. Fig. S7b exhibits the morphology of Bi_2Se_3, which has a 200 nm in diameter. Fig. S7c shows that Sb_2Se_3 has a nanorod morphology. The Bi_2Se_3/Sb_2Se_3@NC@G is fully encapsulated in graphene, proving the successful carbon confinement. The dual confinement approach has been shown to greatly enhance structural integrity, leading to improved long-term cycling performance. The features enhance potassium storage and electron transfer, buffer volume expansion, and prevent K_2Se dissolution in the electrolyte during charge/discharge cycles.

Raman spectra (Figs. S8, S9) show a prominent D band at 1350 cm^{-1}, indicating disordered or defective carbon, and a G band at 1580 cm^{-1}, reflecting graphite carbon. The I_D/I_G ratio of 0.737 for ball milled Bi_2Se_3/Sb_2Se_3@NC@G suggests structural defects and a degree of graphitization, confirming successful graphene encapsulation[45]. Thermal gravimetric analysis (TGA) (Figs. S10, S11) reveals carbon contents of 24.3%, 27.71%, and 21% for Bi_2Se_3/Sb_2Se_3@NC@G, Bi_2Se_3@NC@G, and Sb_2Se_3@NC@G, respectively [46]. Bi_2Se_3/Sb_2Se_3@NC@G exhibits a specific surface area of 10.296 m^2g^{-1} (Fig. S12). The chemical composition of Bi, Sb, Se is 35.13%, 17.83%, 36.03 wt%, respectively by ICP analysis (Table S2). HRTEM images (Fig. 1f) reveal distinct interfaces and lattice structures of Bi_2Se_3 and Sb_2Se_3 within Bi_2Se_3/Sb_2Se_3@NC, demonstrating no phase separation and aligning with XRD findings (Fig. S13). Furthermore, we use geometrical phase analysis (GPA) derived from HTERM confirm the distinct interfaces again (Fig. 1g). High-angle annular dark-field

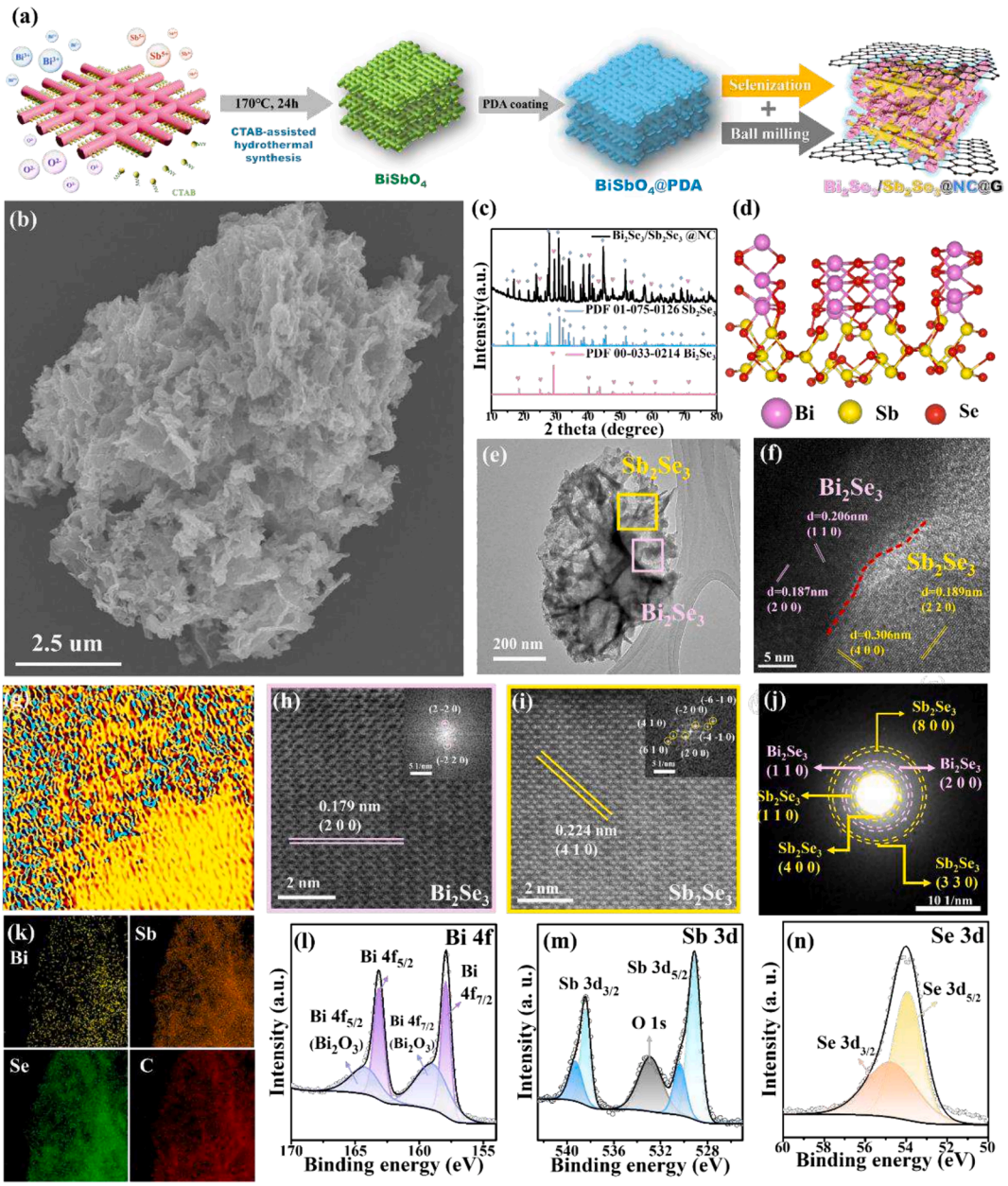

Fig. 1. Material characterization of Bi_2Se_3/Sb_2Se_3@NC. (a) The synthetic route of the Bi_2Se_3/Sb_2Se_3@NC. (b) SEM image, (c) XRD patterns, and (d) Crystal structure of Bi_2Se_3/Sb_2Se_3@NC. (e) TEM images. (f) HRTEM images. (g) GPA derived from HTERM. (h, i) HAADF-STEM images. (j) SAED pattern. (k) EDS elements mapping. (l, m, n) High-resolution XPS spectra of Bi, Sb, and Se.

scanning transmission electron microscopy (HAADF-STEM) images (Fig. 1h–i) display Bi_2Se_3 with a 0.179 nm gap corresponding to the (2 0 0) crystal plane and Sb_2Se_3 with a 0.224 nm gap for the (4 1 0) plane. SAED analysis (Fig. 1j) confirms the polycrystalline nature of Bi_2Se_3/Sb_2Se_3@NC@NC, highlighted by pink and yellow rings indicating various crystal planes of Bi_2Se_3 and Sb_2Se_3, respectively. EDS elemental mapping (Fig. 1k) verifies a uniform distribution of Bi, Sb, Se, and C, further confirming the heterostructure's integrity. Furthermore, Fig. S14 shows the HRTEM image of Bi_2Se_3 in Bi_2Se_3/Sb_2Se_3@NC, Fig. S14b and shows a 0.182 nm gap corresponding to the (2 0 0) crystal plane. The corresponding IFFT images and lattice spacing measured by Gatan Software are provided. Fig. S15 shows the HRTEM image of Sb_2Se_3 in Bi_2Se_3/Sb_2Se_3@NC, Fig. S15b shows a 0.249 nm gap corresponding to the (4 1 0) crystal plane. Fig. S15c and d are the corresponding IFFT image and lattice spacing. XPS analysis (Fig. 1l–n) reveals the elemental valence states and surface composition of Bi_2Se_3/Sb_2Se_3@NC, displaying characteristic spectra for Bi 4f, Sb 3d, and Se 3d. The Bi spectra (Fig. 1l) show peaks at 163.1 and 157.9 eV for Bi $4f_{5/2}$ and Bi $4f_{7/2}$ respectively, with additional peaks indicative of surface is oxidized Bi (Bi_2O_3) [47]. Sb 3d spectrum includes peaks at 538.4 and 529.1 eV for Sb $3d_{3/2}$ and Sb $3d_{5/2}$, representing Sb^{3+}, plus peaks at 539.3 and 530.4 eV from surface oxidation. The Se 3d spectrum (Fig. 1n) shows peaks at 54.8 and 53.9 eV for Se $3d_{3/2}$ and Se $3d_{5/2}$. Fig. S20 reveals the XPS spectra of Bi_2Se_3@NC, the Bi spectra show peaks at 163.3 and 158.1 eV for Bi $4f_{5/2}$ and Bi $4f_{7/2}$ respectively. XPS spectra of Sb_2Se_3@NC shows that Sb 3d spectrum includes peaks at 538.5 and 529.2 eV for Sb $3d_{3/2}$ and Sb $3d_{5/2}$, representing Sb^{3+} (Fig. S21a). The Se 3d spectrum (Fig. S21b) shows peaks at 54.8 and 53.9 eV for Se $3d_{3/2}$ and Se $3d_{5/2}$.

To verify the semiconductor types and the p-n heterojunction, UPS was used to examine the electronic band structures, revealing valence band maximum (VBM) edges at 1.57 eV for Bi_2Se_3@NC and 1.91 eV for Sb_2Se_3@NC, as depicted in Fig. 2a–c [43]. The bandgap of the

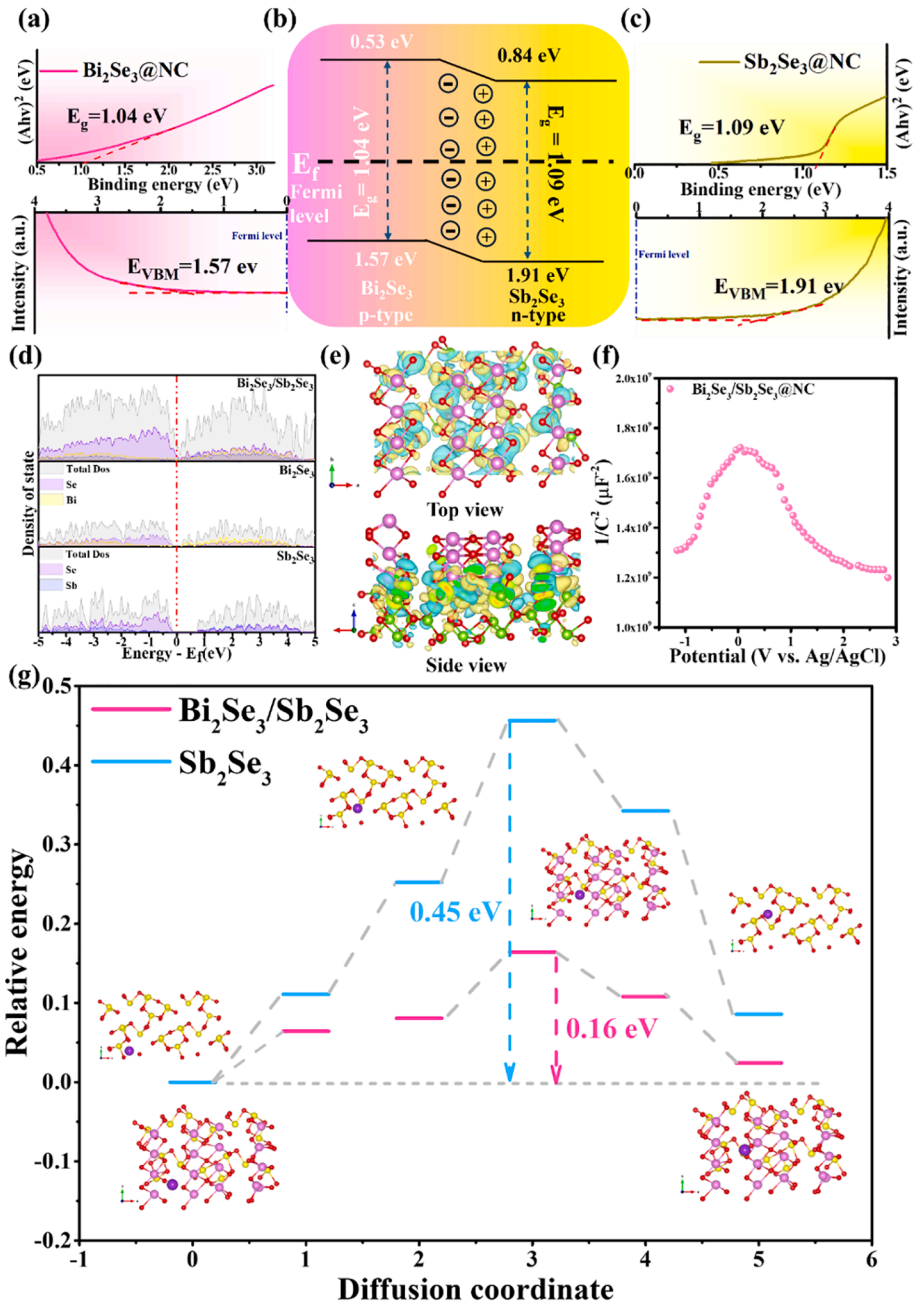

Fig. 2. (a) Tauc's bandgap plots, UPS valence band spectra of Bi_2Se_3@NC. (b) Band diagram. (c) Tauc's bandgap plots, UPS valence band spectra of Sb_2Se_3@NC. (d) Calculated DOS analyses. (e) Charge density difference for Bi_2Se_3/Sb_2Se_3@NC. (f) Mott-Schottky plots of Bi_2Se_3/Sb_2Se_3@NC. (g) Comparison of energy barrier of K^+ diffusion.

Bi_2Se_3@NC and Sb_2Se_3@NC are estimated according to the Tauc's method are 1.04 and 1.09 Ev [48]. Due to the varying positions of the Fermi level, natural electron transfer happens upon contact, resulting in the creation of an intrinsic electric field. The band alignment diagram in Fig. 2b shows that in the p-n heterojunction, holes from p-type Bi_2Se_3 migrate towards n-type Sb_2Se_3, while electrons move from n-type to p-type [45]. Carrier recombination at the interface establishes an equilibrium, forming a depletion region with positive and negative charges [49]. This charge redistribution and depletion zone formation crucially modify the local and electronic structure of the material. Density functional theory (DFT) calculations were used to analyze the density of states (DOS) for Bi_2Se_3, Sb_2Se_3, and their heterostructures, as shown in Fig. 2d [50]. Bi_2Se_3, influenced by topological effects, displays a narrow bandgap, where both conduction and valence bands are predominantly made up of Se-p states with minor contributions from Bi-p states. In contrast, Sb_2Se_3 features a larger bandgap, with its conduction and valence bands also primarily composed of Se-p states, but with slight involvement of Sb-p states. The formation of Bi_2Se_3/Sb_2Se_3 heterostructures significantly enhances conductivity compared to pure Bi_2Se_3 and Sb_2Se_3, improving diffusion dynamics and electrochemical performance. This increase in conductivity is attributed to p-n heterojunctions with built-in electric fields that promote efficient charge transfer. Furthermore, the presence of numerous heterojunctions facilitates K^+ diffusion and electron transfer, thereby augmenting the ion storage capacity in K^+ electrodes. Charge density difference studies, illustrated in Fig. 2e, show electron distributions in depletion (green) and accumulation (yellow) zones, indicating electron movement directions. At the heterojunction interface, electrons diffuse from n-type Sb_2Se_3 to p-type

Bi_2Se_3, aligning the Fermi level. This electron movement enables bidirectional charge transfer, enhances electron transport at the interface, and improves ion diffusion dynamics, thereby boosting the performance and long-term cycling stability of PIB. Fig. S22 shows the charge density difference of Sb_2Se_3. Theoretical calculations corroborate these experimental observations in high-performance PIB systems. The type of a semiconductor can be classified from the slope in the Mott-Schottky plot; a positive slope signifies n-type, while a negative slope signifies p-type (Fig. S23). Fig. 2f, marked by an inverted "V" pattern, verifies the successful formation of an p-n junction with an intrinsic electric field. Furthermore, Mott-Schottky plots at the fully discharged state (0.01 V) demonstrates that the p-n junction still exists at the fully discharged state (Fig. S24). As illustrated in Fig. 2g, the energy barrier of K atoms on the Bi_2Se_3/Sb_2Se_3 are 0.06, 0.08, 0.16, 0.1 eV, which is apparently lower than the Sb_2Se_3. The diffusion barrier of K on Bi_2Se_3/Sb_2Se_3 is three times smaller than Sb_2Se_3, which can be attributed to the built-in electric field generation [51–53]. We compare another diffusion path of Bi_2Se_3/Sb_2Se_3 with Sb_2Se_3 in Fig. S25, confirms the same result that Bi_2Se_3/Sb_2Se_3 has a smaller energy barrier than Sb_2Se_3. Therefore, the construction of the heterostructure enhances charge transfer and ion diffusion during cycling.

Based on the special designed engineering and unique morphology, the impact of the structural design of the Bi_2Se_3/Sb_2Se_3@NC@G was investigated through SEM images under different cycles because the results can reflect the stability of the material and the influence of bond softening. The pristine electrode of Bi_2Se_3/Sb_2Se_3@NC@G showed a smooth surface without any fracture (Fig. 3a). After 250 cycles, the electrode maintained a smooth and integrity surface, thus avoiding the pulverization of active materials (Fig. 3c) [54]. In comparison, the aggregated Sb_2Se_3@NC@G electrode undergo large volume variation and structural collapse after 100 cycles (Fig. 3f) [54,55]. With the increase of cycle numbers, the size of the cracks increases accordingly (Fig. 3g). FEA studies were conducted using the simplest model, which does not include the two-layer carbon. We developed two models to investigate the stress distribution of the morphological Bi_2Se_3/Sb_2Se_3 and Sb_2Se_3 nanorods during potassium insertion. The mechanical properties of Bi_2Se_3 and Sb_2Se_3 are shown in Table S1 [30,56]. The design of the morphological Bi_2Se_3/Sb_2Se_3 model involves Sb_2Se_3 rods encapsulated by Bi_2Se_3, whereas the second model consists of pure Sb_2Se_3 rods. The simulations captured the stress evolution during

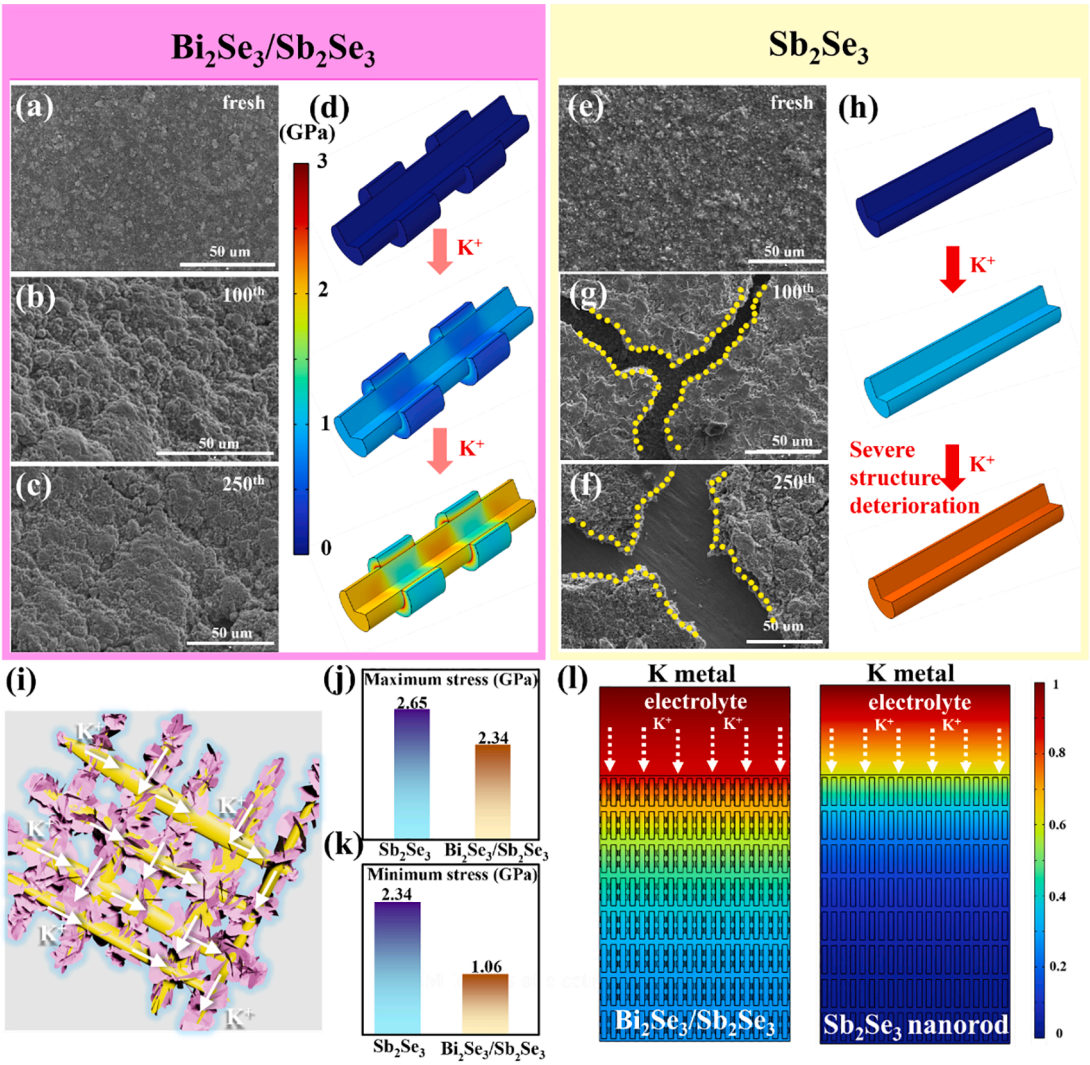

Fig. 3. SEM images of Bi_2Se_3/Sb_2Se_3@NC@G electrode surface before cycling and after cycling: (a) pristine, (b) 100th cycle, (c) 250th cycle. (d) Finite element simulation models of Bi_2Se_3/Sb_2Se_3 with the stress distribution. SEM images of Sb_2Se_3 electrode surface before cycling and after cycling: (e) pristine, (f) 100th cycle, (g) 250th cycle. (h) Finite element simulation models of Sb_2Se_3 with the stress distribution. (i) Schematic illustration of Bi_2Se_3/Sb_2Se_3@NC electrode. (j, k) The maximum and minimum stress of the morphological Bi_2Se_3/Sb_2Se_3 and Sb_2Se_3 nanorod. (l) K^+ concentration distribution for morphological Bi_2Se_3/Sb_2Se_3 and Sb_2Se_3 nanorod.

potassium insertion, with both models transitioning from blue to red, indicating increased stress levels. The morphological Bi_2Se_3/Sb_2Se_3 shows lower stress during potassium insertion, resulting in the material remaining intact (Fig. 3d). On the other hand, the Sb_2Se_3 nanorods experienced higher stress and deformation during potassium insertion, leading to material fracture due to unresolved stresses, which facilitated the formation of a new SEI layer. The newly formed SEI layer would obstruct charge transfer rate (Fig. 3h). The FEA results align with the SEM images after cycling. Fig. S26 shows the SEM images of Bi_2Se_3@NC@G electrode after cycling, which exhibits a similar trend to

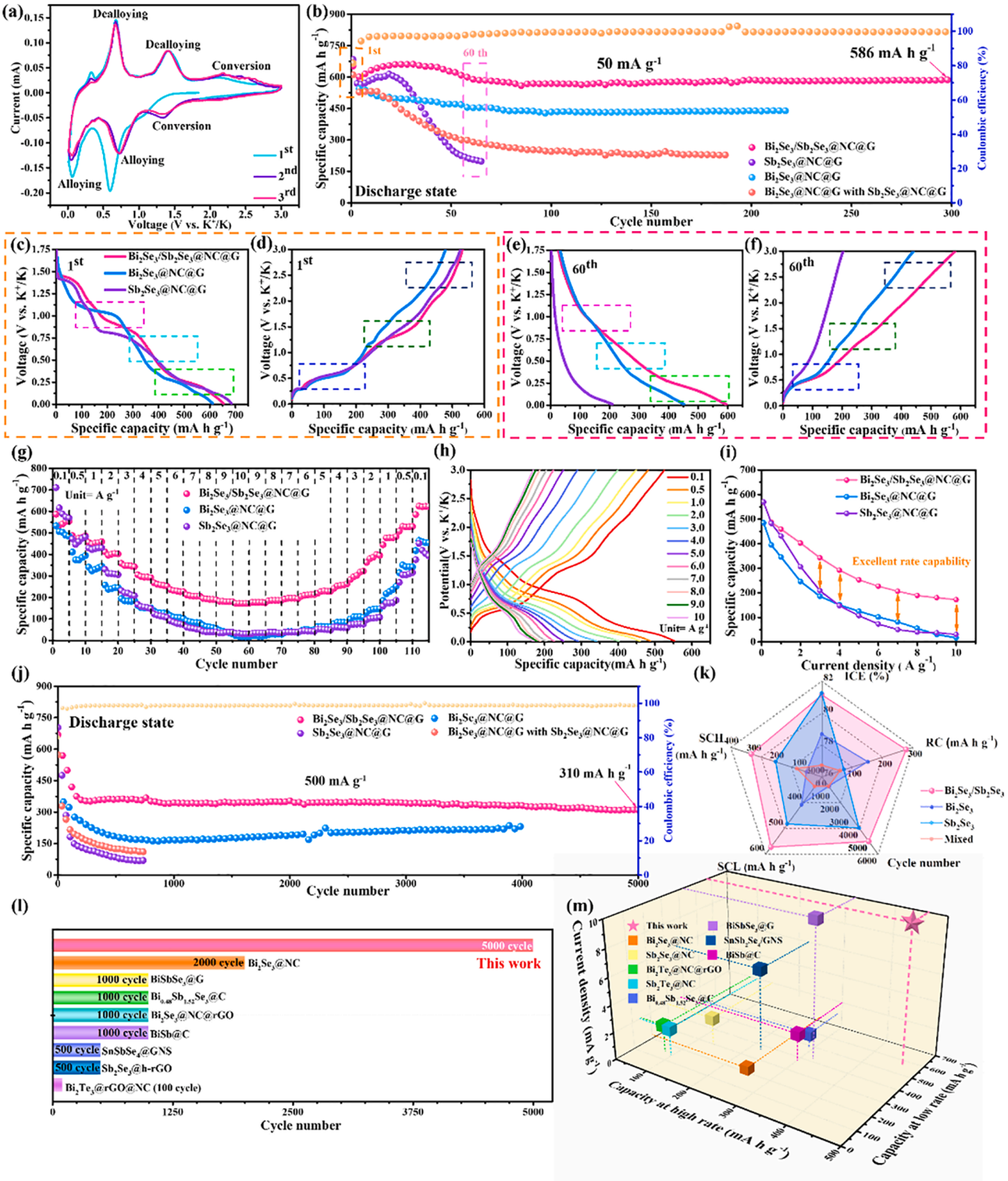

Fig. 4. (a) CV curves at 0.1 mV/s. (b) Cycling performance at 50 mA g^{-1}. (c, d) GCD profiles of the 1st cycle at 50 mA/g. (e, f) GCD profiles of 60th cycle at 50 mA g^{-1}. (g) Rate capability when the current densities are in the range from 0.1 A g^{-1} to 10 A g^{-1}. (h) The corresponding GCD profiles at various rates. (i) The corresponding specific capacities from 0.1 A g^{-1} to 10 A g^{-1}. (j) Long-term cycling performance at 500 mA g^{-1}. (k) ICE, CR, SCL, SCH, and cycle number with previous works. (l) Comparison of cycle number among the Bi_2Se_3/Sb_2Se_3@NC@G and other reported PIBs anodes. (m) Comparison of current density, capacity at high rate, capacity at low rate among the Bi_2Se_3/Sb_2Se_3@NC@G and other reported PIBs anodes.

the fracture tendency of the Sb_2Se_3@NC@G electrode. Fig. 3i is the schematic illustration of the Bi_2Se_3/Sb_2Se_3@NC@G composite, the morphological design can not only relive the stress during charge/discharge, but also enhance the transfer rate by the cross section. The maximum and minimum stresses for Sb_2Se_3 (2.65 GPa and 2.34 GPa, respectively) exceed those of morphological multicomponent Bi_2Se_3/Sb_2Se_3 (2.34 GPa and 1.06 GPa, respectively) (Fig. 3j, k). The findings indicate that the morphological Bi_2Se_3/Sb_2Se_3 structure more effectively alleviates volume expansion compared to the Sb_2Se_3 nanorods during the charge and discharge process. The unique structural features of the morphological Bi_2Se_3/Sb_2Se_3 and the Sb_2Se_3 rods influence their distinct potassium (K^+) diffusion kinetics. Fig. 3l illustrates a more uniform distribution of K^+ concentration in Bi_2Se_3/Sb_2Se_3 compared to Sb_2Se_3, which improves the electrode's wettability in the electrolyte [56]. Uniform electrolyte contact promotes higher Coulombic efficiency, correlating with experimental findings.

Fig. 4a presents the measured CV curve at a scan speed of 0.1 mV s^{-1}, where the CV plot reveals three distinct peaks at 1.3, 0.7, and 0.1 V during the first discharge cycle, indicating a three-step reduction process. The peak voltage at 1.3 V corresponds to the conversion reaction, while 0.7 V and 0.1 V indicate the two-step alloying reaction of Bi and Sb: $(Bi,Sb)\rightarrow K_x(Bi,Sb)\rightarrow K_3(Bi,Sb)$ [57]. The first charge cycle shows three clear peaks at 0.65 V, 1.4 V, and 2.2 V, representing a three-step oxidation process. A notable anodic peak at 0.33 V signifies carbon intercalation. The voltages at 0.65 V and 1.4 V correspond to the two-step dealloying reaction: $K_3(Bi,Sb)\rightarrow K_x(Bi,Sb)\rightarrow(Bi,Sb)$ [58]. Peak overlap in subsequent CV curves demonstrates the high reversibility and stability of the Bi_2Se_3/Sb_2Se_3@NC@G electrode. Fig. S27 displays the CV curves of Bi_2Se_3@NC@G and Sb_2Se_3@NC@G. Fig. 4b shows that the Bi_2Se_3/Sb_2Se_3@NC @G electrode delivers an initial capacity of 668 mA h g^{-1}, a reversible capacity of 583 mA h g^{-1} at 50 mA g^{-1} and maintains a 94.7% capacity retention after 300 cycles. In contrast, the Sb_2Se_3@NC@G electrode starts with a higher capacity of 683 mA h g^{-1} but experiences a dramatic decay after 60 cycles. The Bi_2Se_3@NC@G electrode's capacity quickly declines within the first 30 cycles. The mixture of Bi_2Se_3@NC@G with Sb_2Se_3@NC@G performs poorly, reflecting the intrinsic properties of Bi_2Se_3 and Sb_2Se_3. This suggests that the substantial volume expansion in single metal alloying reactions significantly hampers electrochemical performance.

In the alloying reaction, the Sb_2Se_3@NC@G electrode experiences a volume expansion rate of 407 % due to the formation of K_3Sb [59], significantly impairing its electrochemical performance. Conversely, the Bi_2Se_3/Sb_2Se_3@NC@G electrode can alleviate the volume changes from alloy reaction by synergistic triple-action design. Fig. 4c–f displays the galvanostatic charge–discharge (GCD) curves for the 1st and 60th cycles. For the Sb_2Se_3@NC@G electrode, the conversion reaction occurs at 2.2–1.0 V, involving the reaction $Sb_2Se_3+6K^++6e^-\rightarrow 3K_2Se+2Sb$, and the alloying reaction takes place at 1.0–0.01 V, where $Sb+3K^++3e^-\rightarrow K_3Sb$ [60]. After 60 cycles, the conversion and alloying reactions have almost disappeared in the Sb_2Se_3@NC@G electrode, indicating significant material degradation (Fig. 4e). In contrast, Fig. 4f shows that the Bi_2Se_3@NC@G electrode maintains distinct conversion (K_2Se) and alloying (K_3Bi) reactions [44]. Thanks to the synergistic triple-action design, which enables clear observation of both reaction types in the Bi_2Se_3/Sb_2Se_3@NC@G electrode even after 60 cycles. The Bi_2Se_3/Sb_2Se_3@NC@G electrode demonstrates long-term cycling stability, with outstanding rate performance attributed to its three-dimensional structure. Tested across a range of current densities from 0.1 A g^{-1} to 10A g^{-1}, the electrode's capacity at various current levels shows a decline from 580 mA h g^{-1} at 0.1 A g^{-1} to 172 mA h g^{-1} at 10 A g^{-1}. Remarkably, when the current density is reduced back to 0.1 A g^{-1}, the capacity recovers to 620 mA h g^{-1} (Fig. 4g–h, Fig. S28). This recovery is likely due to structural rearrangement and nanoparticle size reduction during cycling, enhancing material activation [41]. The single-phase Sb_2Se_3@NC@G electrode delivers high capacity but exhibits unstable performance at high current densities, while the Bi_2Se_3@NC electrode maintains stable but lower rate capabilities [61]. Fig. 4i illustrates that the Bi_2Se_3/Sb_2Se_3@NC@G electrode combines Bi_2Se_3's stability with Sb_2Se_3's high specific capacity, offering a balance between rate capacity and cyclability. Fig. 4j demonstrates that the Bi_2Se_3/Sb_2Se_3@NC@G electrode maintains a reversible capacity of 311 mA h g^{-1} and an average Coulombic efficiency of 99.9% even after 5000 cycles at a high rate of 500 mA g^{-1}. The high Coulombic efficiency of the Bi_2Se_3/Sb_2Se_3@NC@G electrode can be attributed to the uniform contact with electrolytes, facilitated by the design of lattice softening and double confinements, which also enhance long-term cycling stability and rapid kinetics during potassiation/depotassiation processes. Fig. S29 displays the cycling performance of the Bi_2Se_3/Sb_2Se_3@NC@G and Bi_2Se_3/Sb_2Se_3@NC electrodes at 0.5 A g^{-1}. The Bi_2Se_3/Sb_2Se_3@NC@G electrode has superior performance compared to Bi_2Se_3/Sb_2Se_3@NC electrode. The reason of the result can be credited to the synergistic effect between the graphene and Bi_2Se_3/Sb_2Se_3@NC. Fig. S30 shows the photographs, SEM images and TEM images of the Bi_2Se_3, Bi_2Se_3/Sb_2Se_3 and Sb_2Se_3 electrodes after 60 cycles at 0.5 A g^{-1}. First, it can be observed that Bi_2Se_3 and Bi_2Se_3/Sb_2Se_3 remained intact (Fig. S30a–e). On the other hand, Sb_2Se_3 electrode showed obvious cracks (Fig. S30g−h). The results are the same as the TEM image (Fig. S30c, f, i). Fig. S30c and f showed nanoparticles encapsulated in graphene uniformly after 60 cycles. In contrast, the Sb_2Se_3 exhibited pulverized fragments after 60 cycles (Fig. S30 i). The reason could be credited to the bond energy of Bi-Se is lower than Sb-Se. According to Guo et al. previous report, the lattice softening effect is caused by the low bond energy. The Bi-Se bond energy is lower than Sb-Se and can avoid the pulverizations caused by volume expansion. The result could explain why there were almost no cracks on the surface of Bi_2Se_3/Sb_2Se_3 electrode (Fig. S30 f), The result of Fig. S30 can correspond to Fig. 4j, the long-term cycling performance could be enhanced by the bond softening effect. It is worth to mention that Bi_2Se_3/Sb_2Se_3 electrode shows superior cycling stability than the mixture Bi_2Se_3 with Sb_2Se_3 which do not have bond softening effect in Fig. 4b and j. We experimented with using DMC instead of DME as the electrolyte in half-cells and tested it at current densities of 0.05 and 0.5 A g^{-1}. The results showed that DMC is unsuitable for K^+ storage in this electrode, as demonstrated in Fig. S31 [31,62]. Fig. S32 shows that pure graphene provides a limited capacity of 88 mA h g^{-1} after 80 cycles at a current density of 500 mA g^{-1}, underscoring its minimal capacity contribution in electrochemical tests. This contrasts with the Bi_2Se_3/Sb_2Se_3 @NC@G electrode, which exhibits excellent cycling stability and rate capability.

Based on the results of the electrochemical tests, the design of the synergistic triple-action morphological composite anode proves beneficial for excellent cycling performance and rapid potassium ion transport rates. Various comparisons were conducted from multiple perspectives, including comparing single materials with multi-materials synthesized using the same method, comparing BiSe-based and SbSe-based materials using different synthesis methods, evaluating the protective effects of different carbon materials, and comparing single synergistic effects with multiple synergistic effects. The findings demonstrate that multiple synergistic effects have a significant impact on electrode development, greatly enhancing electrochemical performance. A radar diagram in Fig. 4k compares all materials across five parameters: initial Coulombic efficiency (ICE), specific capacity at low rate (50 mA g^{-1}, SCL), high rate (500 mA g^{-1}, SCH), cycle number, and capacity retention (CR at 10 A g^{-1}) [42]. Due to irreversible capacity loss in conversion reactions, all materials show an ICE below 80% [63]. The Bi_2Se_3/Sb_2Se_3@NC@G electrode demonstrates superior performance in the remaining four parameters, with discharge capacities 4.4 times and 1.3 times higher than the Sb_2Se_3@NC@G and Bi_2Se_3@NC@G electrodes, respectively. The Sb_2Se_3@NC@G electrode shows poor cycling life and low-capacity retention, which can be attributed to the absence of the bond softening effect (single alloy reaction). The Bi_2Se_3@NC@G electrode presents low capacity because it did not induce Sb, which can contribute large capacity. Fig. 4l highlights the outstanding cycling performance of the

Bi_2Se_3/Sb_2Se_3@NC@G electrode, surpassing most advanced Bi/Sb/Se anodes in potassium ion batteries, such as Sb_2Se_3, $BiSbSe_3$, $SnSbSe_4$, and other alloying and conversion type anode [46,47,60,64–68]. It is noteworthy that most Bi, Sb, Se based electrode have limited cycling performance (<2000 cycles), indicating that the insufficient strategy is not able to tackle the volume expansion and shuttle effect. The excellent performance of Bi_2Se_3/Sb_2Se_3@NC@G electrode can be attributed to the synergistic triple-action design, which can greatly inhibit the material dissolve into the electrolyte, showing superior long-term cycling performance, high capacity, and high-rate performance [31]. A 3D plot in Fig. 4m compares low-rate specific capacity (SCL at 50 mA g^{-1}), high-rate specific capacity (SCH at 500 mA g^{-1}), and rate capability (at 1.0 A g^{-1}), demonstrating the Bi_2Se_3/Sb_2Se_3@NC@G electrode's superior capacity and rate capability. It is worth to mention that the Bi_2Se_3/Sb_2Se_3@NC@G electrode shows astonishing rate capability up to 10 A g^{-1} with the capacity of 172 mA h g^{-1} due to the existence of p-n junction [34,69]. Therefore, the Bi_2Se_3/Sb_2Se_3@NC@G electrode have a higher capacity than (Bi,Sb) based electrode and have a superior cycling performance than selenium based electrode.

The Bi_2Se_3/Sb_2Se_3@NC@G electrode exhibited notable rate capabilities in Fig. 4g and even demonstrate a higher capacity back to 0.1 A g^{-1}. Importantly, we observed that the capacity of Bi_2Se_3/Sb_2Se_3@NC@G after 110 cycles is higher than before 5 cycles, speculating that it can exhibit high reversible rate performance. In addition to electrochemical kinetic testing, the multi-rate performances of four samples from 0.1 A g^{-1} to 5 A g^{-1} are tested with three consecutive times (Fig. 5a) [70]. Based on the consecutive multistep, it can be explored the recovery at the high rate. Therefore, the capacity was 636 mA h g^{-1} upon returning to 0.1 A g^{-1} during the first cycle, 622 mA h g^{-1} in the second cycle, and 584 mA h g^{-1} in the third, demonstrating the highest capacity among all the electrodes. In comparison, the Bi_2Se_3@NC@G electrode and the mixture of Bi_2Se_3@NC@G with Sb_2Se_3@NC@G electrode shows a relative low capacity, and Sb_2Se_3@NC@G presents a fast capacity degradation. Fig. 5b highlights

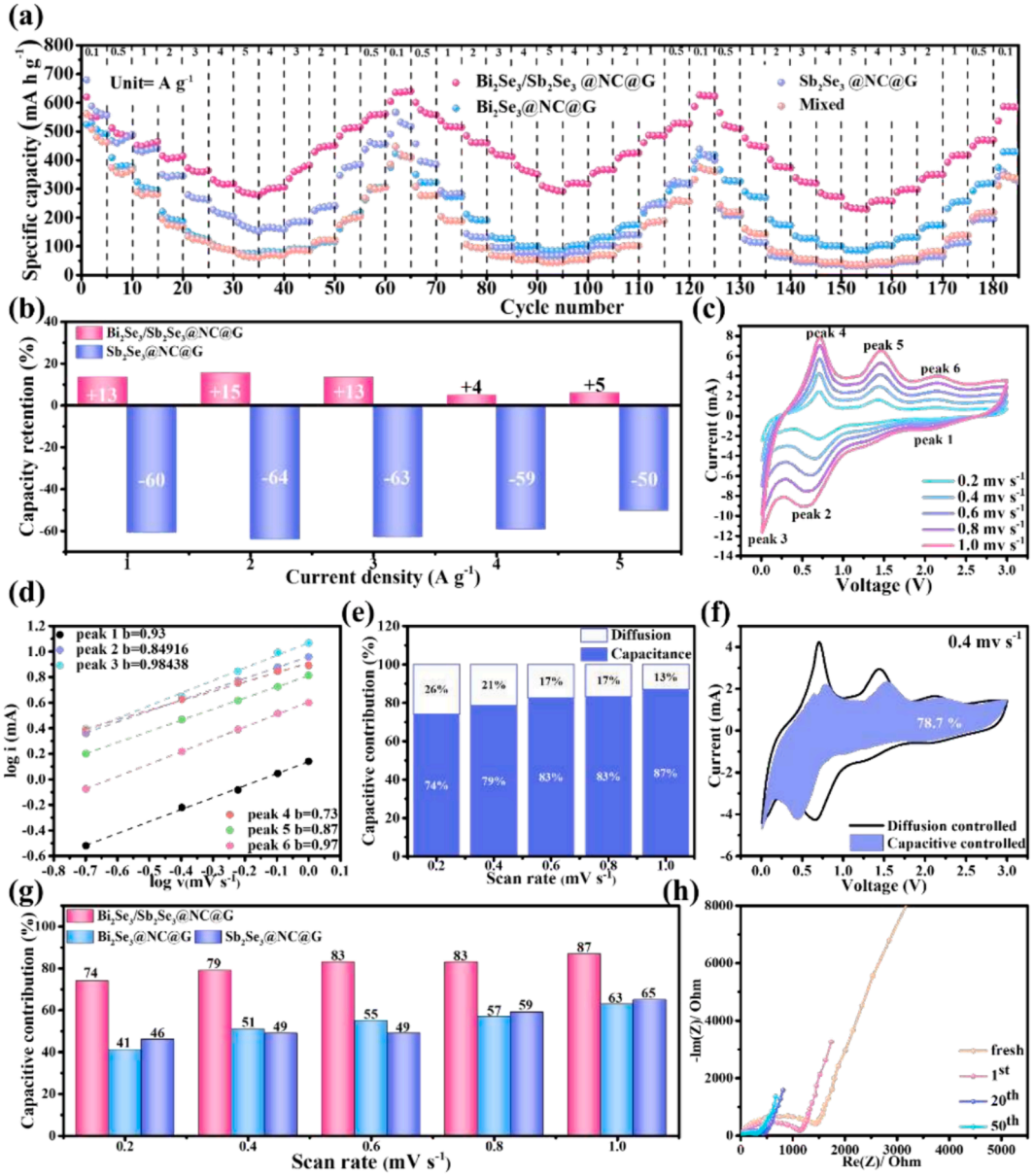

Fig. 5. (a) Three consecutive rate capability tests under the current densities from 0.1 A/g to 5 A g^{-1}. (b) Capacity retention comparison. (c) CV curves at various scan rates in the range of 0.2 – 1.0 mV s^{-1}. (d) Linear relation of log (i, peak current) and log (v, scan rate). (e) Contribution ratio of the capacitive and diffusion-controlled capacities of the Bi_2Se_3/Sb_2Se_3@NC@G electrode. (f) Pseudocapacitive contribution at the scan rate of 0.4 mV s^{-1}. (g) Capacitive-controlled contribution at different scan rates. (h) Nyquist plots before and after cycling test.

the capacity retention between the Bi_2Se_3/Sb_2Se_3@NC@G electrode and Sb_2Se_3@NC@G electrode based on 1–65 cycles and 66–125 cycles. The Sb_2Se_3@NC @G electrode exhibits over 60 % capacity lost when the current density is larger than 1 A g^{-1}. On the contrary, the Bi_2Se_3/Sb_2Se_3@NC@G electrode even demonstrate a higher capacity in 66–125 cycles. This phenomenon is likely attributed to the reduction in nanoparticle size during cycling, which enhances material activation. Despite the dual confinement design of the Sb_2Se_3@NC@G electrode, it still exhibits extremely poor capacity retention. In contrast, the Bi_2Se_3/Sb_2Se_3@NC@G electrode, with its synergistic triple-action design, demonstrates excellent capacity retention.

Fig. 5c analyzes the capacitive effects of the electrode at varying scan rates (0.2–1.0 mV s^{-1}) through CV curves. The increasing shape similarity across higher scan rates confirms stable electrochemical reactions in the Bi_2Se_3/Sb_2Se_3@NC@G electrode, validating its performance in the PIB system [71]. The relationship between peak current (i) and scan rate (ν) in power-law terms is described by $i = a\nu^b$, where a and b are constants. The b value quantifies the degree of capacitive behavior: a value of 0.5 suggests a diffusion-controlled process, whereas a value of 1.0 indicates a capacitive-controlled process [72]. By plotting log(i) against log(ν), b values are determined from the linear slope, with results for peaks 1 to 6 being 0.93, 0.84, 0.98, 0.73, 0.87, and 0.97, respectively (Fig. 5d). The b values calculated for Bi_2Se_3@NC@G and Sb_2Se_3@NC@G are less than 0.7 (Fig. S33). The nearly 0.9'b' values for Bi_2Se_3/Sb_2Se_3@NC@G indicate a pseudocapacitive storage mechanism. The above results confirm that bond softening effect can improve the rate capability. This method allows further quantification of capacitive contributions. The current $i(\nu)$ as a function of scan rate ν is modeled by $i(\nu)=k_1\nu+k_2\nu^{1/2}$, where $k_1\nu$ corresponds to non-Faradaic processes and $k_2\nu^{1/2}$ to Faradaic processes [73]. Fig. 5e shows pseudo-capacitive contributions at scan rates of 0.2, 0.4, 0.6, 0.8, and 1.0 mV s^{-1}, with capacitive ratios of 74 %, 79 %, 83 %, 83 %, and 87 %, respectively. At a lower scan rate of 0.4 mV s^{-1}, the capacitive contribution reaches 78.7 %, indicating a significant pseudo-capacitive storage capacity (Fig. 5f). Fig. 5g and S30 illustrate that the surface capacitance of the Bi_2Se_3/Sb_2Se_3@NC@G electrode has a capacitive contribution larger than 80 %. On the other hand, the Bi_2Se_3@NC@G and Sb_2Se_3@NC@G electrode's capacitive contribution are less than 60 %.

Additionally, the diffusion coefficient of the electrode was assessed using the GITT. After calculation, the diffusion coefficient of the Bi_2Se_3/Sb_2Se_3@NC@G electrode range from 1.4×10^{-11} to 6.18×10^{-10} cm^2 s^{-1} during potassiation and 4.6×10^{-11} to 7×10^{-10} cm^2 s^{-1} during depotassiation (Figs. S34–S35), demonstrating rapid K^+ diffusion due to the electrode's structural properties [74]. Furthermore, the Bi_2Se_3/Sb_2Se_3@NC@G electrode exhibits reduced electrochemical polarization, implying that the voltage variation at steady current is lower during each charging and discharging cycle compared to Sb_2Se_3@NC@G electrode. The Sb_2Se_3@NC@G electrode shows an average smaller diffusion coefficient. These results demonstrate an effective triple-Action design, which lowers the energy barrier and improves the kinetics of the alloying process. Fig. 5h shows a Nyquist plot with depressed semicircles and a diffusion tail, indicating the charge transfer resistance (R_{ct}) at the electrode/electrolyte interface. R_{ct} decreases with increasing cycle number, with lower values suggesting faster charge transfer and higher electronic conductivity[75]. Additionally, in-situ electrochemical impedance spectroscopy (EIS) was used to analyze the electrochemical reactions of the Bi_2Se_3/Sb_2Se_3@NC@G electrode during charging and discharging. In the initial cycle, resistance increases slightly at 1.7 V due to irreversible K^+ insertion, SEI formation, and conversion reactions. Below 1.5 V, resistance significantly drops, linked to the alloying reaction of (Bi,Sb). As charging approaches 0.6 V, resistance further decreases, reflecting the K_3(Bi,Sb) alloying reaction (Fig. S36 a). The Bi_2Se_3@NC@G electrode and Sb_2Se_3@NC@G electrode exhibit a higher resistance compared to the Bi_2Se_3/Sb_2Se_3@NC@G electrode (Fig. S36 b, c). The Bi_2Se_3@NC@G electrode exhibits an increase slightly at 1.6 V due to SEI formation. Below 1.25 V, resistance dramatically drops, linked to the alloying reaction. As charging approaches 0.2 V, resistance further decreases, reflecting the dealloying reaction of K_3Bi (Fig. S36 b). The Sb_2Se_3@NC@G electrode shows a similar resistance change with Bi_2Se_3@NC@G electrode. Operando and ex-situ EIS spectra confirm reduced charge transfer and diffusion barriers during potassium ion insertion/extraction, due to bond softening effect and dual confinement [50,76].

To investigate the bond softening effect and ensure high reversibility of the electrode, we employed a range of analytical techniques, including in situ XRD, ex situ XPS, and ex situ TEM. Bi exhibits a chemical bond softening effect, which can effectively reduce the volume expansion caused by the (Bi,Sb) alloy. Additionally, the (Bi,Sb) alloy structure typically features small nanocrystals (<20 nm) that form a stable matrix [42,77]. These nanocrystals are strategically separated by voids, playing a crucial role in mitigating the effects of volume changes during charge/discharge cycles, thereby enhancing the long-term reversibility of the electrode [47]. By observing the compositional and morphological changes of the materials after cycling, it can be more clearly demonstrated that the introduction of Bi_2Se_3 is beneficial for improving the poor electrochemical performance of Sb_2Se_3. This is visually found in figures showing rod-shaped Sb_2Se_3@NC and Bi_2Se_3/Sb_2Se_3@NC@G fully encapsulated by graphene after ball milling. The in-situ contour mapping of the Bi_2Se_3/Sb_2Se_3@NC electrode, detailed in Fig. 6a, captures the dynamic phase changes during battery operation. As the potential drops to 1.2 V, the appearance of the (Bi,Sb) phase is noted, and upon further discharging to 0.1 V, a new peak corresponding to the K_3(Bi,Sb) phase emerges. This electrode demonstrates high capacity due to the synergistic effects of alloying ((Bi,Sb)) and conversion reactions, achieving a total theoretical capacity of 670 mA h g^{-1} as depicted in Fig. 4f. These results not only confirm the existence of the (Bi,Sb) alloy but also validate the bond softening effect, which effectively relieves volume expansion and provides substantial capacity during prolonged cycling tests. The observed multistep dealloying reaction during the depotassiation process aligns well with the CV results, marking a significant insight into the electrode's performance. Further analysis through ex situ XPS measurements revealed insights into the chemical states and reversibility of the electrode. The distribution of zero-valence species exhibited lower binding energies in the discharged state as compared to the charged state, signifying a reversible reaction between the alloying and metallic phases [42]. Notable peaks at 158.1 and 163.7 eV in the Bi 4f spectrum and at 529.2 eV in the Sb 3d spectrum during the discharge to 0.01 V indicated the occurrence of the alloying reaction, as demonstrated in Fig. 6b and Fig. 6d [78]. Upon recharging to 3.0 V, the disappearance of the Bi peak suggested a transformation involving Bi^{3+} and metallic Bi, a process confirmed by the shifts to higher binding energies shown in Fig. 6e, further confirming the reversible nature of the alloy reaction. To investigate the morphological changes accompanying the phase transformation during discharge and charge cycles and to confirm the existence of K_2Se, extensive ex situ TEM, HRTEM, SAED measurements, and ex situ XRD were performed. In the discharged state (0.01 V), uniformly dispersed small nanoparticles (NPs) were observed, indicating a transition to a smaller grain size. Each nanoparticle, measuring below 10 nm, was closely interconnected, forming a uniformly distributed nanocrystal matrix. Despite the volume changes induced by alloying and dealloying processes, the nanocrystalline aggregate did not pulverize under stress. The interconnection of each nanocrystal, along with the lattice-softening effect in the (Bi,Sb) alloy, significantly enhanced structural integrity. The SAED patterns confirmed the discharge products consisted of K_3(Bi,Sb) and K_2Se, as displayed in Fig. 6g, with lattice fringes corresponding to various planes indicative of these phases. Upon charging to 3.0 V, the nanoparticles remained closely interconnected, forming a uniformly distributed matrix. The structural stability of the nanocrystalline aggregate suggests that stress from volume changes during alloying and dealloying processes did not cause fractures. This stability was confirmed by consistent elemental distribution in EDS mapping and XRD analysis, which showed

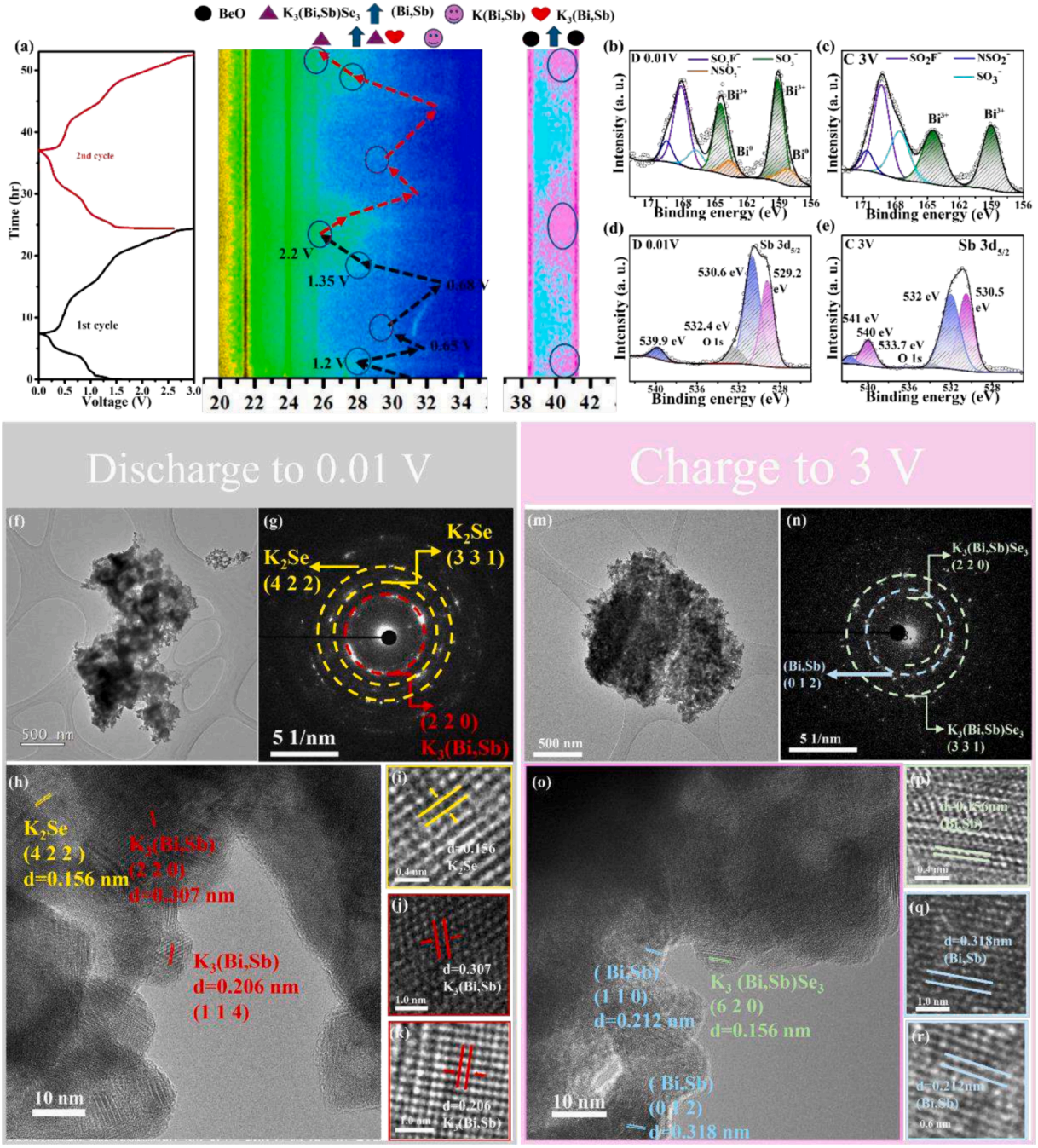

Fig. 6. (a) Contour plot of the operando XRD pattern. (b, c) XPS spectra of Bi 4f (d, e) XPS spectra of Sb 3d after discharging to 0.01 V and charging to 3 V at the initial cycle. (f) Low magnification TEM images after discharging to 0.01 V. (g) SAED patterns. (h, i, j, k) HRTEM images. (l) EDS elements mapping. (f) Low magnification TEM images charged to 3.0 V. (g) SAED patterns. (o, p, q, r) HRTEM images.

an increasing peak intensity at 20° as the discharge approached 0.01 V, indicating the formation of K_2Se (Fig. S37). The stability of this nanoparticle structure helps minimize reactive surface area loss, which is crucial for maintaining capacity over extended cycles.

We developed full cell systems for practical applications in PIB and PIHC using Bi_2Se_3/Sb_2Se_3@NC@G as the anode. PB, synthesized by the co-precipitation method, showed diffraction peaks corresponding to the $K_2Co[Fe(CN)_6]$ crystal phase (PDF no. 31–1000) (Fig. S38), and it can reversibly intercalate K ions without compromising its structure. Due to the high oxidation potential of K_2Se and the inability of organic cathode materials like PTCDA to handle voltages above 3.5 V, high-voltage Prussian analogues were chosen [79]. The full cell, denoted as Bi_2Se_3/Sb_2Se_3@NC@G//PB, was tested between 1.0 and 3.8 V (Fig. 7a). The CV curve (Fig. 7b) shows two redox peaks at 2.11/2.88 V and 2.6/3.2 V, indicating high reversibility. After the third cycle, the CV curves of the Bi_2Se_3/Sb_2Se_3@NC@G//PB full cell overlap, indicating high reversibility and stability. Fig. 7c shows the typical GCD curves for the Bi_2Se_3/Sb_2Se_3@NC@G half-cell, the PB half-cell, and the full cell, consistent with the CV results. Fig. 7d illustrates the rate performance and cycling stability, with the full cell delivering discharge capacities ranging from 384.5 mA h g^{-1} at 0.1 A g^{-1} to 303.4 mA h g^{-1} at 3 A g^{-1}. Notably, the cell maintains over 99% Coulombic efficiency and excellent stability even at high current densities of 3 A g^{-1}. When the current density returns to 0.1 A g^{-1}, the discharge capacity of the Bi_2Se_3/Sb_2Se_3@NC@G//PB full cell immediately recovers to 366 mA h g^{-1}. Following the rate performance test, the battery underwent a cycling

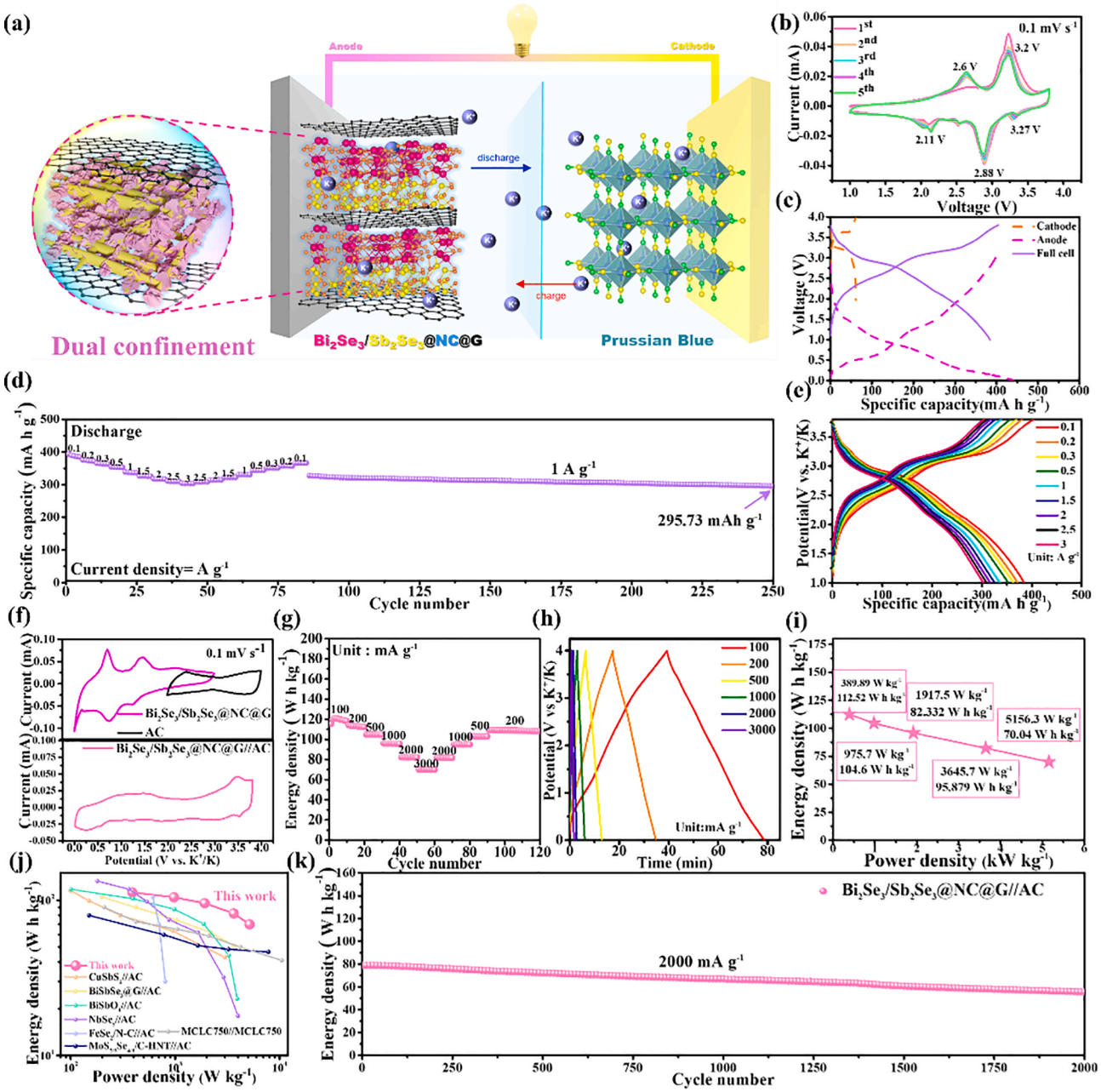

Fig. 7. (a) Schematic diagram of a Bi_2Se_3/Sb_2Se_3@NC@G//PB full cell. (b) CV profiles of the Bi_2Se_3/Sb_2Se_3@NC@G//PB full cell. (c) Charge/discharge curves of PB and Bi_2Se_3/Sb_2Se_3 half cells and a Bi_2Se_3/Sb_2Se_3@NC@G//PB full cell. (d) Rate performance of the Bi_2Se_3/Sb_2Se_3//PB full cell at current densities ranging from 0.1 to 3.0 A g^{-1} and cycling stability at 1.0 A g^{-1}. (e) The charge–discharge profiles of Bi_2Se_3/Sb_2Se_3//PB full cell at rates increased from 0.1 to 3.0 A g^{-1}. (f) CV profiles of AC and Bi_2Se_3/Sb_2Se_3@NC@G half cells (top) and Bi_2Se_3/Sb_2Se_3@NC@G//AC PIHC (bottom). (g) Rate performance of the Bi_2Se_3/Sb_2Se_3@NC@G//AC PIHC at current densities. (h) Charge/discharge curves of the Bi_2Se_3/Sb_2Se_3@NC@G//AC PIHC at various current densities. (i) Energy densities and power densities in Ragone plots. (j) Ragone plots of the Bi_2Se_3/Sb_2Se_3@NC@G//AC PIHC compared with those of PIHCs. (k) Long-term cycling performance of the Bi_2Se_3/Sb_2Se_3@NC@G//AC PIHC.

test at 1000 mA g^{-1}, maintaining a discharge capacity of 295.0 mA h g^{-1} after 250 cycles, with a capacity fade of 0.19% per cycle. Fig. 7e displays the GCD curves at various current densities, showing a slight overpotential at higher currents but still demonstrating excellent rate performance. These results affirm the Bi_2Se_3/Sb_2Se_3@NC@G//PB full cell's outstanding cycling stability and rate capability, highlighting its potential for potassium-ion battery applications.

Inspired by the impressive potassium storage capabilities of the Bi_2Se_3/Sb_2Se_3 @NC@G anode, a PIHC was constructed using commercial activated carbon (AC) as the cathode. This setup capitalizes on the dynamic potassium ion kinetics of the Bi_2Se_3/Sb_2Se_3@NC@G material. Here, FSI ions undergo Faradaic reactions at the anode and engage in adsorption and desorption processes at the cathode, enabling high energy density [80]. To prevent electrolyte decomposition at elevated voltages and maximize energy storage, the operational voltage of the Bi_2Se_3/Sb_2Se_3@NC@G//AC capacitor was limited to a range of 0.01–3.8 V [81]. Fig. 7f shows that the Bi_2Se_3/Sb_2Se_3@NC@G//AC capacitor maintains a nearly rectangular CV profile even at high operating voltages, without significant polarization, contrasting with the sharp redox peaks of the Bi_2Se_3/Sb_2Se_3@NC@G half-cell, indicating typical capacitor behavior. CV curves for the AC // potassium half-cell at varying scan rates from 1.0 to 50 mV s^{-1} are shown in Fig. S39. The

capacitor exhibits energy densities of 118.3, 112.3, 104.5, 95.7, 82.09, and 69.89 Wh kg^{-1} at current densities of 0.1, 0.2, 0.5, 1.0, 2.0, and 3.0 A g^{-1}, respectively, based on the total active mass of Bi_2Se_3/Sb_2Se_3@NC@G and AC (Fig. 7g). When the current density is restored to 200 mA g^{-1}, the energy density returns to 108 Wh kg^{-1}, demonstrating the capacitor's excellent reversibility. Minor variations in the GCD curve slopes within the 3 V range at different current densities suggest both Faradaic and non-Faradaic interactions between the Bi_2Se_3/Sb_2Se_3@NC@G anode and the adsorptive AC cathode, with no significant overpotential shift at high scan rates, indicating a dominant pseudocapacitive behavior in the Bi_2Se_3/Sb_2Se_3@NC@G//AC capacitor (Fig. 7h). Energy and power densities plotted on Ragone plots (Fig. 7j) show that the Bi_2Se_3/Sb_2Se_3@NC@G//AC capacitor outperforms alternative materials such as $CuSbS_2$//AC and BiSbSe$_3$@G//AC [42,47,82–84]. Notably, the capacitor achieved a power density of 70 W kg^{-1} and an energy density of 5156.3 Wh kg^{-1}, which is three times the energy density of $BiSbO_4$//AC at the same power level. Long-term cycling tests showed that the Bi_2Se_3/Sb_2Se_3@NC@G//AC PIHC maintained 70.5% capacity retention after 2000 cycles at 2000 mA g^{-1} (Fig. 7k), demonstrating its potential as a high-performance energy storage device due to rapid ion transport, effective adsorption, and ample active sites.

4. Conclusion

Bi_2Se_3/Sb_2Se_3@NC@G with synergistic triple-action design was used as an anode material for PIBs. The Bi_2Se_3/Sb_2Se_3@NC@G benefits include: 1) heterostructure leads to the inherent electric field, enhancing the reaction kinetics. 2) lattice bond softening can effectively soften the chemical bonds, which could decrease the overall reaction energy. 3) double confinement can effectively mitigate volume expansion and inhibit material dissolved into the electrolyte during the charge/discharge process, thus significantly enhancing long-term cycling performance. It is worthy to note that, coupled with DFT/FEA simulations, multi-morphological heterostructure can not only enhance the conductivity but also facilitates electrolyte infiltration. This above-mentioned design addresses the reversibility and cycling challenges encountered in PIBs compared to single synergistic coupling design, thus obtaining a superior electrochemical performance (5000th cycles). The long-term cycling stability outperforms previously published Bi, Sb, and Se-based anodes. From a fundamental perspective, this study prevents structural pulverization and the continuous formation of a solid electrolyte interface, which significantly enhances the electrochemical performance of multielectron transfer electrodes. In terms of design, this work presents an innovative approach that maximizes the energy storage capacity of potassium-ion batteries. It demonstrates that further exploration into nanoscale structure design and optimization can inspire new ideas for enhancing the performance of advanced energy storage materials.

CRediT authorship contribution statement

Jia-Sheng Lin: Writing – original draft, Data curation, Conceptualization. **Yi-Yen Hsieh:** Formal analysis, Conceptualization. **Kai-Yuan Hsiao:** Methodology, Formal analysis, Data curation. **Yi-Chun Yang:** Writing – review & editing, Supervision, Formal analysis. **Che-Hung Wang:** Methodology, Formal analysis, Data curation. **Ming-Yen Lu:** Resources, Data curation. **Wen-Wei Wu:** Visualization, Software, Resources. **Hsing-Yu Tuan:** Writing – review & editing, Writing – original draft, Supervision.

Declaration of competing interest

The authors declare that they have no known competing financial interests or personal relationships that could have appeared to influence the work reported in this paper.

Data availability

No data was used for the research described in the article.

Acknowledgements

This work was supported by the financial support from the 2030 Cross Generation Young Scholars Program by National Science and Technology Council, Taiwan (NSTC 112-2628-E-007-010 & NSTC 112-2628-E-007-016).

Appendix A. Supplementary data

Supplementary data to this article can be found online at https://doi.org/10.1016/j.cej.2024.155370.

References

[1] X. Min, J. Xiao, M. Fang, W.A. Wang, Y. Zhao, Y. Liu, A.M. Abdelkader, K. Xi, R. V. Kumar, Z. Huang, Potassium-ion batteries: outlook on present and future technologies, Energ. Environ. Sci. 14 (2021) 2186–2243.
[2] K. Chayambuka, G. Mulder, D.L. Danilov, P.H. Notten, Sodium-ion battery materials and electrochemical properties reviewed, Adv. Energy Mater. 8 (2018) 1800079.
[3] J. Sun, F. Kang, D. Yan, T. Ding, Y. Wang, X. Zhou, Q. Zhang, Recent Progress in Using Covalent Organic Frameworks to Stabilize Metal Anodes for Highly-Efficient Rechargeable Batteries, Angew. Chem. Int. Ed. (2024) e202406511.
[4] S. Chen, J. Zhong, H. Deng, Q. Wei, X. Shen, X. Jia, S. Li, Q. Zhang, J. Zhu, B. Lu, Advanced potassium-ion batteries with high areal capacity, CCS Chemistry 6 (2024) 1011–1023.
[5] X. Jia, S. Li, S. Chen, L. Wang, H. Deng, Y. Yuan, H. Sun, L. Fu, J. Zhu, B. Lu, Covalently bonded metal-organic groups anodes for high-performance potassium-ion batteries, Sci. China Mater. 66 (2023) 3827–3836.
[6] Y. Liang, W.H. Lai, Z. Miao, S.L. Chou, Nanocomposite materials for the sodium–ion battery: a review, Small 14 (2018) 1702514.
[7] S. Liu, L. Kang, J. Henzie, J. Zhang, J. Ha, M.A. Amin, M.S.A. Hossain, S.C. Jun, Y. Yamauchi, Recent advances and perspectives of battery-type anode materials for potassium ion storage, ACS Nano 15 (2021) 18931–18973.
[8] Y. Xu, Y. Du, H. Chen, J. Chen, T. Ding, D. Sun, D.H. Kim, Z. Lin, X. Zhou, Recent advances in rational design for high-performance potassium-ion batteries, Chem. Soc. Rev. (2024).
[9] C. Zhang, H. Zhao, Y. Lei, Recent research progress of anode materials for potassium-ion batteries, Energy & Environmental Materials 3 (2020) 105–120.
[10] L. Zhang, W. Wang, S. Lu, Y. Xiang, Carbon anode materials: a detailed comparison between Na-ion and K-ion batteries, Adv. Energy Mater. 11 (2021) 2003640.
[11] F. Yang, Z. Liu, D. Wang, K. Hui, Y. Zhang, Z. Peng, Preparation and properties of P-Bi2Te3/MXene superstructure-based anode for potassium-ion battery, Acta Physico-Chim Sin 40 (2023) 2303006.
[12] S. Li, H. Chen, Q. Zhang, H. Deng, S. Chen, X. Shen, Y. Yuan, Y. Ding, Y. Cheng, H. Sun, Enhanced potassium-ion storage performance of bimetallic-sulfide based on regulatory reaction mechanism, Chem. Eng. J. 466 (2023) 143342.
[13] Y. Yuan, S. Wang, S. Li, S. Chen, H. Deng, X. Jia, Q. Zhang, W. Chen, Q. Zhao, Z. Liu, In situ synthesis of Fe7Se8 with a yolk-shell structure achieves fast and stabilized potassium storage, Cell Reports Physical Science 4 (2023).
[14] H. Deng, L. Wang, S. Li, M. Zhang, T. Wang, J. Zhou, M. Chen, S. Chen, J. Cao, Q. Zhang, Radial pores in nitrogen/oxygen dual-doped carbon nanospheres anode boost high-power and ultrastable potassium-ion batteries, Adv. Funct. Mater. 31 (2021) 2107246.
[15] S. Chong T. Li S. Qiao Y.-C. Yang Z. Liu J. Yang H.-Y. Tuan G. Cao W. Huang Boosting Manganese Selenide Anode for Superior Sodium-Ion Storage via Triggering α→ β Phase Transition 2024 ACS nano.
[16] Y.-X. Huang, F. Wu, R.-J. Chen, Thermodynamic analysis and kinetic optimization of high-energy batteries based on multi-electron reactions, Natl. Sci. Rev. 7 (2020) 1367–1386.
[17] R. Chen, R. Luo, Y. Huang, F. Wu, L. Li, Advanced high energy density secondary batteries with multi-electron reaction materials, Adv. Sci. 3 (2016) 1600051.
[18] Y. Liu, Q. Wan, J. Gong, Z. Liu, G. Tao, J. Zhao, L. Chen, W. Li, X. Wei, L. Ni, Confine, Defect, and Interface Manipulation of Fe3Se4/3D Graphene Targeting Fast and Stable Potassium-Ion Storage, Small 19 (2023) 2206400.
[19] W. Feng, X. Wei, F. Cao, Y. Li, X. Zhang, Y. Li, W. Liu, J. Han, D. Kong, L. Zhi, Defective MoSSe with local-expanded structure for high-rate potassium ion battery, Energy Storage Mater. 65 (2024) 103186.
[20] Y. Gan, L. Liu, Q. Zhang, J. Huang, S. Han, B. Chen, Y. Liu, Q. Yu, L. Guan, T. Zhou, Internal interface engineering of yolk-shell structure toward fast and robust potassium storage, Energy Storage Mater. 59 (2023) 102794.
[21] X. Gu, L. Zhang, W. Zhang, S. Liu, S. Wen, X. Mao, P. Dai, L. Li, D. Liu, X. Zhao, A CoSe–C@ C core–shell structure with stable potassium storage performance realized by an effective solid electrolyte interphase layer, J. Mater. Chem. A 9 (2021) 11397–11404.
[22] N. Ren, L. Wang, J. Dong, K. Cao, Y. Li, F. Chen, J. Xiao, B. Pan, C. Chen, Synergistic engineering of electronic structure and particle size in SnSe@ CNF

anode toward high performance potassium ion batteries, Chem. Eng. J. 458 (2023) 141489.
[23] C. Zhang, H. Li, X. Zeng, S. Xi, R. Wang, L. Zhang, G. Liang, K. Davey, Y. Liu, L. Zhang, Accelerated diffusion kinetics in ZnTe/CoTe2 heterojunctions for high rate potassium storage, Adv. Energy Mater. 12 (2022) 2202577.
[24] H. Lei, J. Li, X. Zhang, L. Ma, Z. Ji, Z. Wang, L. Pan, S. Tan, W. Mai, A review of hard carbon anode: Rational design and advanced characterization in potassium ion batteries, InfoMat 4 (2022) e12272.
[25] H. Huang, R. Xu, Y. Feng, S. Zeng, Y. Jiang, H. Wang, W. Luo, Y. Yu, Sodium/potassium-ion batteries: boosting the rate capability and cycle life by combining morphology, defect and structure engineering, Adv. Mater. 32 (2020) 1904320.
[26] S. Guo, H. Li, Y. Lu, Z. Liu, X. Hu, Lattice softening enables highly reversible sodium storage in anti-pulverization Bi–Sb alloy/carbon nanofibers, Energy Storage Mater. 27 (2020) 270–278.
[27] U. Szeluga, B. Kumanek, B. Trzebicka, Synergy in hybrid polymer/nanocarbon composites, A Review, Composites Part a: Applied Science and Manufacturing 73 (2015) 204–231.
[28] Q. Xu, J. Qiao, Z. Ren, J. Sun, G. Zhang, L. Li, Multi synergistic coupling design for broadband sound absorption based on compact porous composite embedded with massless membrane resonator, Compos. Struct. 286 (2022) 115312.
[29] L. Wen Q. Zhang J. Shi F. Wang S. Wang Z. Chen Y. Yue Y. Gao Layered Topological Insulator MnBi2Te4 as a Cathode for a High Rate Performance Aqueous Zinc-Ion 2024 Battery, ACS nano.
[30] Y. Wu, Z. Wang, Z. Wang, X. Liu, S. Zhang, C. Deng, Tailoring stress-relieved structure for ternary cobalt phosphoselenide@ N/P codoped carbon towards high-performance potassium-ion hybrid capacitors and potassium-ion batteries, Energy Storage Mater. 57 (2023) 180–194.
[31] R. Hu, D. Sha, X. Cao, C. Lu, Y. Wei, L. Pan, Z. Sun, Anchoring Metal-Organic Framework-Derived ZnTe@ C onto Elastic Ti3C2Tx MXene with 0D/2D Dual Confinement for Ultrastable Potassium-Ion Storage, Adv. Energy Mater. 12 (2022) 2203118.
[32] J. Gong, R. Zhang, X. Wei, Y. Liu, Q. Luo, Q. Wan, Q. Zheng, L. Wang, S. Liu, D. Lin, Spatially dual-confined metallic selenide double active centers for boosting potassium ion storage, Chem. Eng. J. 459 (2023) 141609.
[33] H. Wu, X. Chen, X. Zhang, Z. Jiang, Y. Dong, H. Li, L. Ni, G. Diao, M. Chen, Multidimensional nanobox structural carbon nanofibers with dual confined effect for boosting storage performance and electrochemical kinetics of alkali metal ion batteries, Chem. Eng. J. 428 (2022) 131207.
[34] Q. Cheng, X. Liu, Q. Deng, C. Chen, W. Zhong, C. Yang, Heterostructured Ni3S4/Co9S8 encapsulated in nitrogen-doped carbon nanocubes for advanced potassium storage, Chem. Eng. J. 446 (2022) 136829.
[35] B. Yue, L. Wang, N. Zhang, Y. Xie, W. Yu, Q. Ma, J. Wang, G. Liu, X. Dong, Dual-Confinement Effect of Nanocages@ Nanotubes Suppresses Polysulfide Shuttle Effect for High-Performance Lithium-Sulfur Batteries, Small 20 (2024) 2308603.
[36] X. Ren, Q. Wang, Y. Pu, Q. Sun, W. Sun, L. Lu, Synergizing Spatial Confinement and Dual-Metal Catalysis to Boost Sulfur Kinetics in Lithium-Sulfur Batteries, Adv. Mater. 35 (2023) 2304120.
[37] G. Kresse, D. Joubert, From ultrasoft pseudopotentials to the projector augmented-wave method, Phys. Rev. B 59 (1999) 1758.
[38] S. Grimme, J. Antony, S. Ehrlich, H. Krieg, A consistent and accurate ab initio parametrization of density functional dispersion correction (DFT-D) for the 94 elements H-Pu, J. Chem. Phys. 132 (2010).
[39] J.P. Perdew, K. Burke, M. Ernzerhof, Generalized gradient approximation made simple, Phys. Rev. Lett. 77 (1996) 3865.
[40] R. Fan, C. Zhao, J. Ma, J. Wu, T. He, Y. Dong, J. Dai, Y. Cai, Rich Self-Generated Phase Boundaries of Heterostructured VS4/Bi2S3@ C Nanorods for Long Lifespan Sodium-Ion Batteries, Small 18 (2022) 2205175.
[41] Q. Huang, W. Su, G. Zhong, K. Xu, C. Yang, Bimetal heterostructure NiCo2Se4 anode confined by carbon nano boxes for ultrafast and stable potassium storage, Chem. Eng. J. 460 (2023) 141875.
[42] C.-H. Chang, K.-T. Chen, Y.-Y. Hsieh, C.-B. Chang, H.-Y. Tuan, Crystal facet and architecture engineering of metal oxide nanonetwork anodes for high-performance potassium ion batteries and hybrid capacitors, ACS Nano 16 (2022) 1486–1501.
[43] S.-S. Mai, K.-Y. Hsiao, Y.-C. Yang, Y.-R. Lu, M.-Y. Lu, Y.-Y. Hsieh, C.-B. Chang, H.-Y. Tuan, Synchronous regulation of Schottky/pn dual junction in Prussian blue-derived Janus heterostructures: A path to ultrafast long life potassium ion batteries, Chem. Eng. J. 474 (2023) 145992.
[44] K.-T. Chen, S. Chong, L. Yuan, Y.-C. Yang, H.-Y. Tuan, Conversion-alloying dual mechanism anode: Nitrogen-doped carbon-coated Bi2Se3 wrapped with graphene for superior potassium-ion storage, Energy Storage Mater. 39 (2021) 239–249.
[45] W.W. Shen, Y.Y. Hsieh, Y.C. Yang, K.Y. Hsiao, M.Y. Lu, C.W. Chou, H.Y. Tuan, Thermodynamic Origin-Based In Situ Electrochemical Construction of Reversible p-n Heterojunctions for Optimal Stability in Potassium Ion Storage, Adv. Sci. 2308582 (2024).
[46] T. Yuan, J. Yan, Q. Zhang, Y. Su, S. Xie, B. Lu, J. Huang, X. Ouyang, Unveiling the nature of ultrastable potassium storage in Bi0. 48Sb1. 52Se3 composite, ACS Nano 17 (2023) 10462–10473.
[47] W.-C. Lin, Y.-C. Yang, H.-Y. Tuan, Ternary chalcogenide anodes for high-performance potassium-ion batteries and hybrid capacitors via composition-mediated bond softening and intermediate phase, Energy Storage Mater. 51 (2022) 38–53.
[48] H. Li, C. Chen, Y. Yan, T. Yan, C. Cheng, D. Sun, L. Zhang, Utilizing the Built-in Electric Field of p–n Junctions to Spatially Propel the Stepwise Polysulfide Conversion in Lithium-Sulfur Batteries, Adv. Mater. 33 (2021) 2105067.
[49] Y.-Y. Hsieh, H.-Y. Tuan, Architectural van der Waals Bi2S3/Bi2Se3 topological heterostructure as a superior potassium-ion storage material, Energy Storage Mater. 51 (2022) 789–805.
[50] L. Song, S. Zhang, L. Duan, R. Li, Y. Xu, J. Liao, L. Sun, X. Zhou, Z. Guo, Tunable Interfacial Electric Field-Mediated Cobalt-Doped FeSe/Fe3Se4 Heterostructure for High-Efficiency Potassium Storage, Angew. Chem. Int. Ed. (2024) e202405648.
[51] J. Huang, Y. Yao, M. Huang, Y. Zhang, Y. Xie, M. Li, L. Yang, X. Wei, Z. Li, Creating unidirectional fast ion diffusion channels in G/NiS2-MoS2 heterostructures for high-performance sodium-ion batteries, Small 18 (2022) 2200782.
[52] L. Duan, H. Tang, X. Xu, J. Liao, X. Li, G. Zhou, X. Zhou, MnFe Prussian blue analogue-derived P3-K0. 5Mn0. 67Fe0. 33O1. 95N0. 05 cathode material for high-performance potassium-ion batteries, Energy Storage Materials 62 (2023) 102950.
[53] W. Han, X.W. Gao, Y. Song, X. Wang, G. Gao, H. Chen, Q. Gu, W.B. Luo, Synergistic Effect of Co-Mo Pinning in Lay-Structured Oxide Cathode for Enhancing Stability toward Potassium-Ion Batteries, Small 2400252 (2024).
[54] B. Zhang, B. Xu, Z. Xiao, L. Cao, H. Geng, X. Ou, Inner-stress-dissipative, rapid self-healing core-shell sulfide quantum dots for remarkable potassium-ion storage, Energy Storage Mater. 56 (2023) 96–107.
[55] C.-Y. Tsai, C.-H. Chang, T.-L. Kao, K.-T. Chen, H.-Y. Tuan, Shape matters: SnP0. 94 teardrop nanorods with boosted performance for potassium ion storage, Chem. Eng. J. 417 (2021) 128552.
[56] S. Zhang, F. Ling, L. Wang, R. Xu, M. Ma, X. Cheng, R. Bai, Y. Shao, H. Huang, D. Li, An Open-Ended Ni3S2–Co9S8 Heterostructures Nanocage Anode with Enhanced Reaction Kinetics for Superior Potassium-Ion Batteries, Adv. Mater. 34 (2022) 2201420.
[57] X. Liu, X. Wang, Y. Zhou, B. Wang, L. Zhao, H. Zheng, J. Wang, J. Liu, J. Liu, Y. Li, Novel Ultra-Stable 2D SbBi Alloy Structure with Precise Regulation Ratio Enables Long-Stable Potassium/Lithium-Ion Storage, Adv. Mater. 36 (2024) 2308447.
[58] Y. Liu, F. Liu, B. Liu, Y. Xiao, G. Qin, J. Ma, Dynamic Hydrogen-Bond Network as a Modulator of Bismuth-Antimony Complex Anodes for Self-Healable and Wider Temperature Adaptive Potassium Ion Batteries, Angew. Chem. Int. Ed. 62 (2023) e202300599.
[59] Z. Yi, Y. Qian, S. Jiang, Y. Li, N. Lin, Y. Qian, Self-wrinkled graphene as a mechanical buffer: A rational design to boost the K-ion storage performance of Sb2Se3 nanoparticles, Chem. Eng. J. 379 (2020) 122352.
[60] Z. Yang, W. Li, G. Zhang, J. Wang, J. Zuo, Q. Xu, H. Shan, X. He, M. Lv, J. Hu, Constructing SbOC bond to improve the alloying reaction reversibility of free-standing Sb2Se3 nanorods for potassium-ion batteries, Nano Energy 93 (2022) 106764.
[61] B. Sheng, L. Wang, H. Huang, H. Yang, R. Xu, X. Wu, Y. Yu, Boosting potassium storage by integration advantageous of defect engineering and spatial confinement: a case study of Sb2Se3, Small 16 (2020) 2005272.
[62] L. Zhang, X. Gu, X. Mao, S. Wen, P. Dai, L. Li, D. Liu, X. Zhao, Boosting fast and stable potassium storage of iron selenide/carbon nanocomposites by electrolyte salt and solvent chemistry, J. Power Sources 486 (2021) 229373.
[63] L. Yang, L. Guo, D. Yan, Y. Wang, T. Shen, D.-S. Li, M.E. Pam, Y. Shi, H.Y. Yang, Understanding the highly reversible potassium storage of hollow ternary (Bi-Sb) 2S3@ NC nanocube, ACS Nano 17 (2023) 6754–6769.
[64] S. Chong, S. Qiao, L. Yuan, Q. Zhou, T. Li, S. Dong, Y. Wang, M. Ma, W. Huang, Sb2Te3 hexagonal nanoplates as conversion-alloying anode materials for superior potassium-ion storage via physicochemical confinement effect of dual carbon matrix, Chem. Eng. J. 461 (2023) 141957.
[65] S. Chong, L. Yuan, Q. Zhou, Y. Wang, S. Qiao, T. Li, M. Ma, B. Yuan, Z. Liu, Bismuth Telluride Nanoplates Hierarchically Confined by Graphene and N-Doped C as Conversion-Alloying Anode Materials for Potassium-Ion Batteries, Small 19 (2023) 2303985.
[66] X. Sun, B. Zhang, M. Chen, L. Wang, D. Wang, R. Man, S. Iqbal, F. Tian, Y. Qian, L. Xu, Space-confined growth of Bi2Se3 nanosheets encapsulated in N-doped carbon shell lollipop-like composite for full/half potassium-ion and lithium-ion batteries, Nano Today 43 (2022) 101408.
[67] R. Tian, L. Duan, Y. Xu, Y. Man, J. Sun, J. Bao, X. Zhou, Coupling Ternary Selenide SnSb2Se4 with Graphene Nanosheets for High-Performance Potassium-Ion Batteries, Energy & Environmental Materials 6 (2023) e12617.
[68] Q. Wu, B. Chen, H. Xie, X. Bai, M. Liang, Z. Wu, X. Jin, C. He, N. Zhao, Bismuth-antimony alloy nanoparticles encapsulated in 3D carbon framework: Synergistic effect for enhancing interfacial potassium storage, Chem. Eng. J. 430 (2022) 132906.
[69] L. Cao, B. Luo, B. Xu, J. Zhang, C. Wang, Z. Xiao, S. Li, Y. Li, B. Zhang, G. Zou, Stabilizing intermediate phases via efficient entrapment effects of layered VS4/SnS@ C heterostructure for ultralong lifespan potassium-ion batteries, Adv. Funct. Mater. 31 (2021) 2103802.
[70] H. Li, Y. He, Q. Wang, S. Gu, L. Wang, J. Yu, G. Zhou, L. Xu, SnSe2/NiSe2@ N-Doped Carbon Yolk-Shell Heterostructure Construction and Selenium Vacancies Engineering for Ultrastable Sodium-Ion Storage, Adv. Energy Mater. 13 (2023) 2302901.
[71] T. Nagaura, J. Li, J.F. Fernando, A. Ashok, A. Alowasheeir, A.K. Nanjundan, S. Lee, D.V. Golberg, J. Na, Y. Yamauchi, Expeditious Electrochemical Synthesis of Mesoporous Chalcogenide Flakes: Mesoporous Cu2Se as a Potential High-Rate Anode for Sodium-Ion Battery, Small 18 (2022) 2106629.
[72] Y. Liu, Y. Qing, B. Zhou, L. Wang, B. Pu, X. Zhou, Y. Wang, M. Zhang, J. Bai, Q. Tang, Yolk–shell Sb@ void@ graphdiyne nanoboxes for high-rate and long cycle life sodium-ion batteries, ACS Nano 17 (2023) 2431–2439.
[73] Z. Zhang, Q. Hu, J. Liao, Y. Xu, L. Duan, R. Tian, Y. Du, J. Shen, X. Zhou, Uniform P2–K0. 6CoO2 microcubes as a high-energy cathode material for potassium-ion batteries, Nano Lett. 23 (2023) 694–700.

[74] X. Yang, Y. Gao, L. Fan, A.M. Rao, J. Zhou, B. Lu, Skin-Inspired Conversion Anodes for High-Capacity and Stable Potassium Ion Batteries, Adv. Energy Mater. 13 (2023) 2302589.
[75] H. Lu, Z. Zhang, X. An, J. Feng, S. Xiong, B. Xi, In situ electrochemically transforming VN/V2O3 heterostructure to highly reversible V2NO for excellent zinc ion storage, Small Structures 4 (2023) 2300191.
[76] P. Hu, T. Zhu, C. Cai, X. Wang, L. Zhang, L. Mai, L. Zhou, A High-Energy NASICON-Type Na3. 2MnTi0. 8V0. 2 (PO4) 3 Cathode Material with Reversible 3.2-Electron Redox Reaction for Sodium-Ion Batteries, Angewandte Chemie 135 (2023) e202219304.
[77] K.-T. Chen, Y.-C. Yang, L.-M. Lyu, M.-Y. Lu, H.-Y. Tuan, In situ formed robust submicron-sized nanocrystalline aggregates enable highly-reversible potassium ion storage, Nano Energy 88 (2021) 106233.
[78] L. Guo, L. Cao, J. Huang, J. Li, K. Kajiyoshi, J. He, H. Qi, Guiding fabrication of continuous carbon-confined Sb2Se3 nanoparticle structure for durable potassium-storage performance, ACS Applied Energy Materials 4 (2021) 10391–10403.
[79] C. Zhang, Y. Xu, M. Zhou, L. Liang, H. Dong, M. Wu, Y. Yang, Y. Lei, Potassium Prussian blue nanoparticles: a low-cost cathode material for potassium-ion batteries, Adv. Funct. Mater. 27 (2017) 1604307.
[80] M. Chen, L. Wang, X. Sheng, T. Wang, J. Zhou, S. Li, X. Shen, M. Zhang, Q. Zhang, X. Yu, An ultrastable nonaqueous potassium-ion hybrid capacitor, Adv. Funct. Mater. 30 (2020) 2004247.
[81] G. Wang, J. Peng, W. Zhang, Q. Li, Z. Liang, J. Wu, W. Fan, J. Wang, S. Dou, S. Huang, Te-vacancy-rich CoTe2− x anodes for efficient potassium-ion storage, Chem. Eng. J. 149436 (2024).
[82] C.-B. Chang, K.-T. Chen, H.-Y. Tuan, Large-scale synthesis of few-layered copper antimony sulfide nanosheets as electrode materials for high-rate potassium-ion storage, J. Colloid Interface Sci. 608 (2022) 984–994.
[83] H. Min, M. Li, H. Shu, X. Zhang, T. Hu, W. Wang, Y. Zhou, J. Jian, X. Wang, FeSe2 nanoparticle embedded in 3D honeycomb-like N-doped carbon architectures coupled with electrolytes engineering boost superior potassium ion storage, Electrochim. Acta 366 (2021) 137381.
[84] L. Zhong, X. Qiu, S. Yang, S. Sun, L. Chen, W. Zhang, Supermolecule-regulated synthesis strategy of general biomass-derived highly nitrogen-doped carbons toward potassium-ion hybrid capacitors with enhanced performances, Energy Storage Mater. 61 (2023) 102887.